UFC

UNIVERSIDADE FEDERAL DO CEARÁ
CENTRO DE CIÊNCIAS
DEPARTAMENTO DE FÍSICA
PROGRAMA DE PÓS-GRADUAÇÃO EM FÍSICA

Bruno Gondim de Melo Vieira

Plasmonic Properties of Metallic Nanoparticle Layers

Fortaleza - CE, Brasil
2019

Bruno Gondim de Melo Vieira

Plasmonic Properties of Metallic Nanoparticle Layers

Ph.D. thesis presented to the Post-Graduation Course in Physics of the Federal University of Ceará as part of the requisites for obtaining the Degree of Doctor in Physics.

Advisor:
Prof. Dr. Eduardo Bedê Barros

Co-Advisor:
Prof. Dr. Stephanie Reich

Fortaleza - CE, Brasil
2019

Dados Internacionais de Catalogação na Publicação
Universidade Federal do Ceará
Biblioteca Universitária
Gerada automaticamente pelo módulo Catalog, mediante os dados fornecidos pelo(a) autor(a)

V713p Vieira, Bruno Gondim de Melo.
Plasmonic properties of metallic nanoparticle layers / Bruno Gondim de Melo Vieira. – 2019.
77 f. : il. color.

Tese (doutorado) – Universidade Federal do Ceará, Centro de Ciências, Programa de Pós-Graduação em Física , Fortaleza, 2019.
Orientação: Prof. Dr. Eduardo Bedê Barros.
Coorientação: Profa. Dra. Stephanie Reich.

1. plasmon escuro. 2. diferenças finitas no domínio do tempo. 3. espectroscopia de microabsorbância. 4. nanopartículas de ouro e prata. 5. automontagem. I. Título.

CDD 530

Bruno Gondim de Melo Vieira

Plasmonic Properties of Metallic Nanoparticle Layers

Tese submetida à Coordenação do Curso de Pós-Graduação em Física, da Universidade Federal do Ceará, como requisito parcial para a obtenção do grau de Doutor em Física

Aprovada em 14/08/2019 .

BANCA EXAMINADORA

Prof. Dr. Eduardo Bedê Barros (Orientador)
Universidade Federal do Ceará (UFC)

Prof. Dr. Antônio Gomes de Souza Filho
Universidade Federal do Ceará (UFC)

Prof. Dr. Alexandre Rocha Paschoal
Universidade Federal do Ceará (UFC)

Prof. Dr. Stephanie Reich
Freie Universität Berlin (FU-Berlin)

Prof. Dr. Leonardo de Souza Menezes
Universidade Federal de Pernambuco (UFPE)

Dedicated to my parents, Humberto and Luziana,
and my life partner, Cristina.

Acknowledgements

This thesis is the outcome of a tremendous group work. First of all, I would like to thank my long-term advisor, Prof. Eduardo Bedê Barros, for the guidance, the fruitful discussions and for always trusting in my capacity. During my stay in Berlin, Germany, I was fortunately embraced by the research group of Prof. Stephanie Reich. The AG-Reich taught me how collaboration is essential for marvelous scientific achievements. I express deeply my gratitude to Prof. Reich for welcoming me in her group, for all the patience, the guidance and for showing me this amazing area of nanoplasmonics. In special, I also thank Niclas S. Mueller for all the great discussions, the wonderful collaboration and for helping me to understanding the details about this formerly new field to me. In advance, I thank to all other members of my defense committee, Professors Antônio Gomes de Souza Filho, Alexandre Rocha Paschoal and Leonardo de Souza Menezes for their disposal to review this thesis and provide valuable corrections, comments and discussions that will surely improve the quality of this work.

Last but not least, I warmly thank to my father, Humberto, and my mother, Luziana, which are my great example of perseverance and love, and my life partner, Cristina, for all the patience, comprehension and for being on my side in all moments (even when 8000 km were separating us). Thank you for your unconditional support and care. I further thank AGEAC for the sublime teachings that constantly inspires me to become a better person and that have been essential to bring me calm, patience and focus even in the darkest hours.

Finally, I would like to acknowledge the Physics Department of UFC and the Physics Department of FU-Berlin, together with all their staff and all the agencies that provided me financial support: Coordenação de Aperfeiçoamento de Pessoal de Nivel Superior (CAPES) and Dahlem Research School (DRS). This study was financed in part by the Coordenação de Aperfeiçoamento de Pessoal de Nível Superior - Brasil (CAPES) - Finance Code 001.

"To attain knowledge, add things everyday.
To attain wisdom, remove things everyday."

Lao-Tsé

Abstract

Agglomerates of metallic nanoparticles (NPs) are known for a long time to interact remarkably with light, which leads them to a wide range of applications, from high-resolution imaging to solar cells. The self-assembly technique has drawn attention lately as it allows the synthesis of very close-packed nanoparticle clusters with high parameters precision and relatively low cost. This thesis provides a thorough theoretical investigation of the optical properties of mono-, bi- and few-layers made of gold and silver nanoparticles, showing also crucial experimental results that solidly support the study. Finite-difference time-domain (FDTD) simulations predict the excitation of one bright plasmon mode at the monolayers and two plasmon modes at the bilayers, one bright and one dark mode, identified by the parallel and antiparallel induced dipoles between the layers, respectively. A plane linearly polarized incident wave with propagation normal to the film is used. The dark mode excitation is allowed by field retardation that becomes dominant when the size of the nanoparticles is sufficiently large. The spectral properties of the mode, such as resonance energy and linewidth, can be tuned by changing the nanoparticles sizes and their separation. The simulations predict also a high density of nearfield hotspots with intensity enhancement of up to 3000, which indicates that these materials are excellent for spectroscopy applications. Microabsorbance measurements on gold bi- and trilayers show the characteristic absorbance peak from the dark interlayer modes, confirming the simulation predictions. For other few-layers with higher layer numbers, new dark plasmon modes are excited and a standing wave behavior starts to emerge, in which most of the light gets passed through the material and is no longer absorbed. We investigate the possibility of employing the layers for hot-electron generation, providing both FDTD simulations and time-resolved transient absorption experiments. Furthermore, we observe that placing the layers onto a reflective surface leads to a tremendous increase in the optical absorption of the dark modes. All methods we used are very reproducible and the simulated results can be verified experimentally with a relatively simple setup. This study opens the way for many new explorations in both fundamental and applied research.

Keywords: self-assembly, gold nanoparticles, silver nanoparticles, bilayer, few-layers, dark plasmon, finite-difference time-domain (FDTD) simulations, micro-absorbance spectroscopy.

Resumo

Os aglomerados de nanopartículas (NPs) metálicas são conhecidos há muito tempo por sua notável interação com a luz, o que os leva a uma vasta gama de aplicações, desde imagens de alta resolução até células solares. A técnica de automontagem (*self-assembly*) tem chamado atenção ultimamente, já que ela permite a síntese de aglomerados de nanopartículas altamente compactados com alta precisão de parâmetros e custo relativamente baixo. Esta tese fornece uma investigação teórica aprofundada das propriedades ópticas de mono-, bi- e poucas camadas feitas de nanopartículas de ouro e prata, em que se mostra também resultados experimentais cruciais ao embasamento sólido do estudo. Simulações com o método de diferenças finitas no domínio do tempo (FDTD) preveem a excitação de um modo de plasmon claro nas monocamadas e dois modos de plasmon nas bicamadas, um claro e um escuro, identificados pelos dipolos induzidos paralela e antiparalelamente entre as camadas, respectivamente. Nos cálculos, utilizou-se uma onda incidente linearmente polarizada com propagação normal ao filme. A excitação do modo escuro é permitida pelo efeito de retardo de campo, que se torna dominante quando o tamanho das nanopartículas é suficientemente grande. As propriedades espectrais do modo, tais como energia de ressonância e largura de linha, podem ser ajustadas alterando-se os tamanhos das nanopartículas e sua separação. As simulações preveem também uma alta densidade de *hotspots* com aumento de intensidade de campo próximo de até 3000, o que indica que esses materiais são excelentes para aplicações em espectroscopia. As medições de microabsorbância em bi- e tricamadas de ouro mostram o pico de absorbância característico dos modos escuros, confirmando as previsões da simulação. Para estruturas com um maior número de camadas, novos modos de plasmon escuros são excitados e um comportamento de onda estacionária começa a emergir, que faz com que a maior parte da luz passe pelo material e não seja mais absorvida. Investigou-se também a possibilidade de empregar esses materiais na geração de elétrons quentes (*hot-electrons*), em que se apresenta simulações de FDTD e experimentos de absorção transiente resolvidos no tempo. Além disso, observamos que a deposição das camadas em uma superfície refletora leva a um tremendo aumento na absorção óptica dos modos escuros. Vale ressaltar que todos os métodos utilizados são reprodutíveis e os resultados simulados podem ser verificados experimentalmente com uma aparelhagem relativamente simples. Esse estudo abre caminho para muitas novas explorações, tanto em pesquisa fundamental quanto em aplicada.

Palavras-chave: automontagem, nanopartículas de ouro, nanopartículas de prata, bicamada, poucas camadas, plasmon escuro, diferenças finitas no domínio do tempo (FDTD), espectroscopia de microabsorbância.

Contents

List of Figures

List of Tables

List of Abbreviations and Acronyms

CS	Cross-Section
FDTD	Finite-Difference Time-Domain
FWHM	Full Width at Half Maximum
IT	Interband Transitions
LSPPs	Localized Surface Plasmon-Polaritons
LSPR	Localized Surface Plasmon Resonance
MIM	Metal-Insulator-Metal
NP	Nanoparticle
PSPPs	Propagating Surface Plasmon-Polaritons
QSA	Quasi-Static Approximation
TEM	Transmission Electron Microscopy

1 Introduction

Noble-metal nanoparticles (NMNPs) have been studied for many years due to the unique way in which they interact with light. The interaction is mediated by the free electrons inside the nanoparticles (NPs) that are collectively excited by the incident light, which is known as a localized surface plasmon resonance (LSPR)[1,2]. These resonances are strongly dependent on the structural parameters of the nanoparticles, such as shape and size[3]. Due to the strong electric nearfield generated by those excitations in the vicinity of the NMNPs, there is a remarkable enhancement of the optical properties of any material that is close to the metal surface. Consequently, the NMNPs are considered to be excellent systems for applications in high-resolution imaging beyond the diffraction limit[4] and in spectroscopy techniques, such as, fluorescence[5], infrared absorption[6] and Surface-Enhanced Raman scattering (SERS)[7–10]. In fact, there are many other areas in which the NMNPs may be employed, for instance, in optoelectronic devices, as they can shape the light patterns on the nanoscale[11], in biological and chemical sensing[12], in signal-processing systems[4] and in photovoltaic devices[13].

Beyond single nanoparticle systems, it is also possible to cluster nanoparticles together to form more complex structures, bringing up a whole branch of possibilities of novel materials. Due to the coupling between the plasmon modes of each individual particle, ensembles of NMNPs are known to have optical properties that differ from those of individual NPs and their corresponding bulk materials[14,15]. Their optical properties can be additionally tuned by changing the particles distance and arrangement. The self-assembly of NMNPs is an attractive synthesis technique for close-packed ensembles of NPs. The control over structural parameters has been greatly improved in the past years[16–22], as it can be observed in Fig. 1. For instance, Schulz *et al.*[17] were able to synthesize large films (hundreds of μm^2) of close-packed gold nanospheres with particle sizes of up to 46 nm and interparticle distances of 2 nm with a precision of 0.5 nm, see Fig. 1(b). Besides being a relatively low cost synthesis method in comparison to electron-beam lithography, it is very versatile, as many different molecules can be used as ligands to achieve various gap sizes and join together particles with a wide range of sizes. In addition, as those NP films extend over length scales far beyond the diffraction limit, optical measurements can be easily done on them without the need of complex experimental apparatus[23,24].

The optical properties of close-packed ensembles of metallic NPs has been subject in a number of theoretical works. Tao *et al.*[22] considered polyhedral silver NPs colloids of up to three layers and investigated their optical response in both low density and high density configurations. Alaeian and Dionne[25] studied spherical and octahedral NPs superlattices

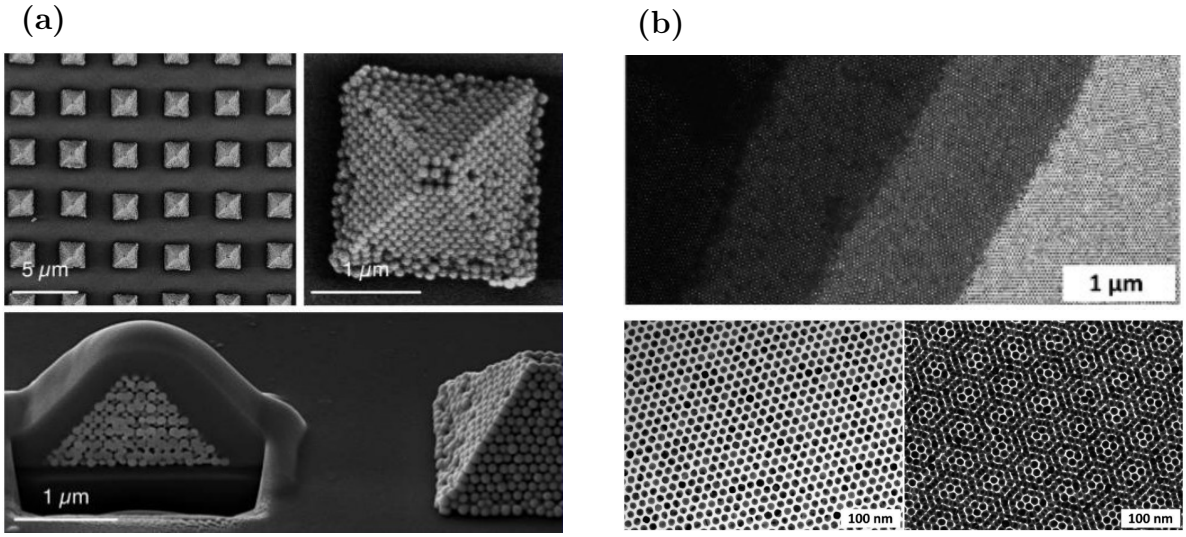

Figure 1: Example of samples produced with the self-assembly technique: **(a)** Pyramidal supercrystals made with gold nanospheres[19] and **(b)** Layers of hexagonal lattices made with gold nanospheres[17].

and showed that they behave as metamaterials with magnetic response. Our recent studies also provided some theoretical analysis on the self-assembly of NMNPs, but the focus was mostly on experimental measurements and potential applications of these materials[23,24]. Furthermore, there is a number of theoretical studies on arrays of metal-insulator-metal particles (MIMs)[26–30]. Although the MIMs are synthesized in a process different from the self-assembly, their optical response has similarities with the response of close-packed NP bilayers, which makes them great to compare with. Although the interest in NMNP layers increases and the development of self-assembly techniques improves at a rapid pace, there is still a lack of a systematic theoretical investigations on the role of geometrical parameters on the plasmonic properties.

This thesis aims to provide a in-depth investigation about the plasmonic properties of layered structures of gold and silver NPs both theoretically and experimentally. The main focus is on the properties of mono- and bilayers, which are the fundamental building blocks for more complex layered structures; however, analysis of up to pentalayers are presented. From finite-difference time-domain (FDTD) simulations, we predict that the monolayers have one plasmon mode, characterized by a non-zero net dipole moment (bright mode), and the bilayers enable the excitation of a bright mode and a second mode that has a vanishing dipole moment (dark mode). This dark mode is activated due to field retardation, that induces an anti-parallel dipole configuration between the layers. The plasmonic modes can be excited by illumination with a plane electromagnetic wave at normal incidence and the optical response is polarization insensitive. We emphasize that dark plasmon modes are receiving considerable attention lately because their vanishing dipole moment makes them less susceptible to radiative losses[29,31–41].

We provide a systematic study on the influence of the structural parameters, including particles size (diameter), their separation (gap) and particle arrangement. From the size analysis, we were able to predict the minimum diameter for which the dark mode is activated. By an analysis of the local nearfield enhancement, we demonstrate the potential of the NP layers for surface-enhanced spectroscopy.[42] By performing micro-absorbance measurements in samples of self-assembly of NPs, the simulation predictions were confirmed[17,23]. The dark modes were excited in colloidal bi- and trilayers of gold NPs and evolved into standing wave patterns with an almost perfect light transmission as more layers are stacked up. Through time-resolved pump-probe spectroscopy, we also demonstrate that these materials are very promising for hot-electron generation. We were even able to predict the particle size that should optimize the hot-electron production.

This thesis is divided in 5 chapters, being the first chapter this introduction. In chapter 2, we present all the fundamental physical concepts that are needed to understand the following chapters. The details of both theoretical and experimental techniques used are described in chapter 3. In chapter 4, the results and discussions are showed, in which all simulated results of mono- and bilayers (Sects. 4.2 and 4.3) together with the experimental observation (Sect. 4.4). Finally, we draw the conclusions and offer perspectives in chapter 5.

2 Theoretical Background

In this chapter, we will briefly address the fundamental theoretical topics that are important to understand the phenomena studied in this thesis. Most of the concepts discussed below were based on the books by Ru and Etchegoin[1], Maier[2] and Novotny and Hecht[43]. They are excellent textbooks for anyone who is interested in further details about plasmonics in general, providing many details on concepts, theoretical models, experiments and applications.

2.1 Drude Model and Introduction to Plasmons

Before introducing the concept of plasmons, let us first understand what happens when electromagnetic waves travel inside a metallic medium. Consider the medium as a gas of free electrons with density n (electrons per unit of volume) that moves in a background of fixed positive ion cores. When an external AC electric field $\boldsymbol{E}$ is applied, the electron gas oscillates in response to it and the motion of a single electron can be described by the following equation*:

$$m\frac{d^2\boldsymbol{r}}{dt^2} + m\gamma\frac{d\boldsymbol{r}}{dt} = -e\boldsymbol{E}, \tag{2.1}$$

where m is the effective optical mass of the electron and e is the elementary charge. γ is the collision frequency of the electrons with the lattice and impurities, which corresponds to a damping in the electron motion. Assuming a harmonic time dependence, $\boldsymbol{E}(t) = \boldsymbol{E}_0 e^{-i\omega t}$, equation 2.1 can be solved by considering $\boldsymbol{r}(t) = \boldsymbol{r}_0 e^{-i\omega t}$, obtaining

$$\boldsymbol{r}_0 = \frac{e}{m(\omega^2 + i\gamma\omega)}\boldsymbol{E}_0. \tag{2.2}$$

As the macroscopic polarization is $\boldsymbol{P} = -ne\boldsymbol{r}$, the electric displacement field $\boldsymbol{D} = \epsilon_0\boldsymbol{E} + \boldsymbol{P}$ in the medium is given by

$$\boldsymbol{D} = \epsilon_0\left(1 - \frac{\omega_p^2}{\omega^2 + i\gamma\omega}\right)\boldsymbol{E} \tag{2.3}$$

As we have that $\boldsymbol{D} = \epsilon_0\epsilon(\omega)\boldsymbol{E}$, the dielectric function of the free electron gas is then determined as

$$\epsilon(\omega) = 1 - \frac{\omega_p^2}{\omega^2 + i\gamma\omega}, \tag{2.4}$$

*As the electrons are not bound, there is no term related to a restoring force (or natural frequency ω_0).

where $\omega_p = \sqrt{\frac{ne^2}{\epsilon_0 m}}$ is called the *plasma frequency* and defined as oscillation frequency of the free electron charge density.[1,2]

The contribution of the ion cores can be included by considering them as an medium with an effective constant real dielectric function ϵ_∞. This assumption means that an additional polarization term $P_\infty = \epsilon_0(\epsilon_\infty - 1)\boldsymbol{E}$ has to be inserted to eq. (2.4), that becomes

$$\epsilon(\omega) = \epsilon_\infty - \frac{\omega_p^2}{\omega^2 + i\gamma\omega}. \tag{2.5}$$

This dielectric function in eq. (2.5) represents the fundamental way in which metallic media react in the presence of electromagnetic waves. This approach for finding $\epsilon(\omega)$ is called *plasma model* or *Drude model* of the optical response of metals.

The real and imaginary parts of eq. (2.5) are given by

$$\begin{cases} \mathrm{Re}[\epsilon(\omega)] = \epsilon_\infty - \dfrac{\omega_p^2}{\omega^2 + \gamma^2}, \\ \mathrm{Im}[\epsilon(\omega)] = \dfrac{\omega_p^2 \gamma}{\omega(\omega^2 + \gamma^2)}. \end{cases} \tag{2.6}$$

As the damping factor γ is normally much smaller than the typical incident light frequencies (ω) used in these studies, we have that $\mathrm{Re}[\epsilon(\omega)] \approx 0$ for $\omega = \frac{\omega_p}{\epsilon_\infty}$ and that $\mathrm{Re}[\epsilon(\omega)] < 0$ when ω decreases further. If ω is not far below $\frac{\omega_p}{\epsilon_\infty}$, $\mathrm{Im}[\epsilon(\omega)]$ is relatively small (compared to smaller ω). This frequency region in which we have the combination of negative $\mathrm{Re}[\epsilon(\omega)]$ and small $\mathrm{Im}[\epsilon(\omega)]$ is where interesting optical effects, including plasmonic resonances, occur. The continuous decrease of $\mathrm{Re}[\epsilon(\omega)]$ towards negative values is an attribute of all metals and one of their most crucial characteristics, at least with respect to optical properties. Many of the known optical properties of metals involves this negativity of $\mathrm{Re}[\epsilon(\omega)]$ at visible wavelengths, such as being excellent reflectors.[1]

Despite its simplicity, the Drude model is actually very useful to predict the optical response of real metals in specific wavelength ranges, besides being very instructive to understand the problem. Fig. 2 shows the comparison between the Drude dielectric function with the real dielectric function of gold, taken from the experiments made by Johnson and Christy[44]. It is evident that the Drude model agrees pretty well to the real gold values for energies below 2 eV but it fails for higher frequencies.† This disagreement comes mainly from the fact that the Drude model considers just intraband optical transitions in their formalism, since all electrons in the free electron gas remain in the same electronic band, i.e. the conduction band. In real metals, on the other hand,

†The energy values are related to the frequency ω by the Planck constant $\hbar$ ($E = \hbar\omega$). The terms energy and frequency are being used interchangeably.

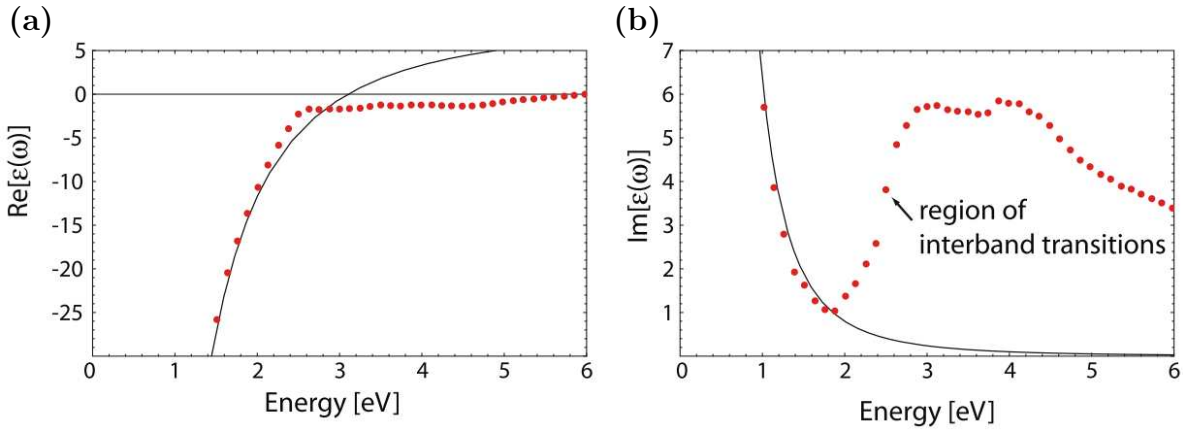

Figure 2: **(a)** Real and **(b)** imaginary parts of the Drude dielectric function $\epsilon(\omega)$ as function of the photon energy ($\hbar\omega$). The values of ϵ_∞, ω_p and γ were used to fit eq. (2.5) to the experimental data for the dielectric function of gold (red dots)[44]. There is a clear energy position ($\approx$ 2 eV) above which the Drude model is no longer valid.[2]

the optical excitation of bound electrons to higher energy bands may also occur. Such processes are known as *interband transitions* (IT) and can be described approximately as a sequence of Lorentz oscillators. With IT contributions, the dielectric function assumes the following general form:

$$\epsilon(\omega) = \epsilon_b(\omega) - \frac{\omega_p^2}{\omega^2 + i\gamma\omega}, \tag{2.7}$$

in which $\epsilon_b(\omega)$ represents the interband transitions. If the transitions occur at much higher energies than ω_p, the $\epsilon_b(\omega)$ term can be approximated to the constant dielectric ϵ_∞ and eq. (2.7) turns into eq. (2.5). However, if the IT are close to or below ω_p, a more complex expression for $\epsilon_b(\omega)$ is necessary to account for the details of the band-like nature of these transitions. This situation is the observed for gold in Fig. 2.

At this point, maybe it is clear that a plasmon is related to the oscillations of the free charges in metals. According to Ru and Etchegoin[1], a plasmon can be formally defined as "a quantum quasi-particle representing the elementary excitations, or modes, of the charge density oscillations in a plasma." Despite the reference to quantum mechanics in this definition, plasmons can be investigated without the quantum theory. This definition might be better explained by tracing a parallel with photons. In the same way a photon is a particle that represents elementary excitations (modes) of electromagnetic waves, a plasmon represents elementary modes in the free electron gas density. In other words, plasmons are for the plasma charge density in a metal the same that photons are for light. The main difference is that plasmons are always subject to many sorts of damping that makes them decay over time and/or space while photons normally have an indefinitely long lifetime. Plasmons are then known as quasi-particles to distinguished them from real quantum particles, such as photons. Although plasmons are closely related to the electronic oscillations, the plasmonic behavior of a metal can be fully studied through its

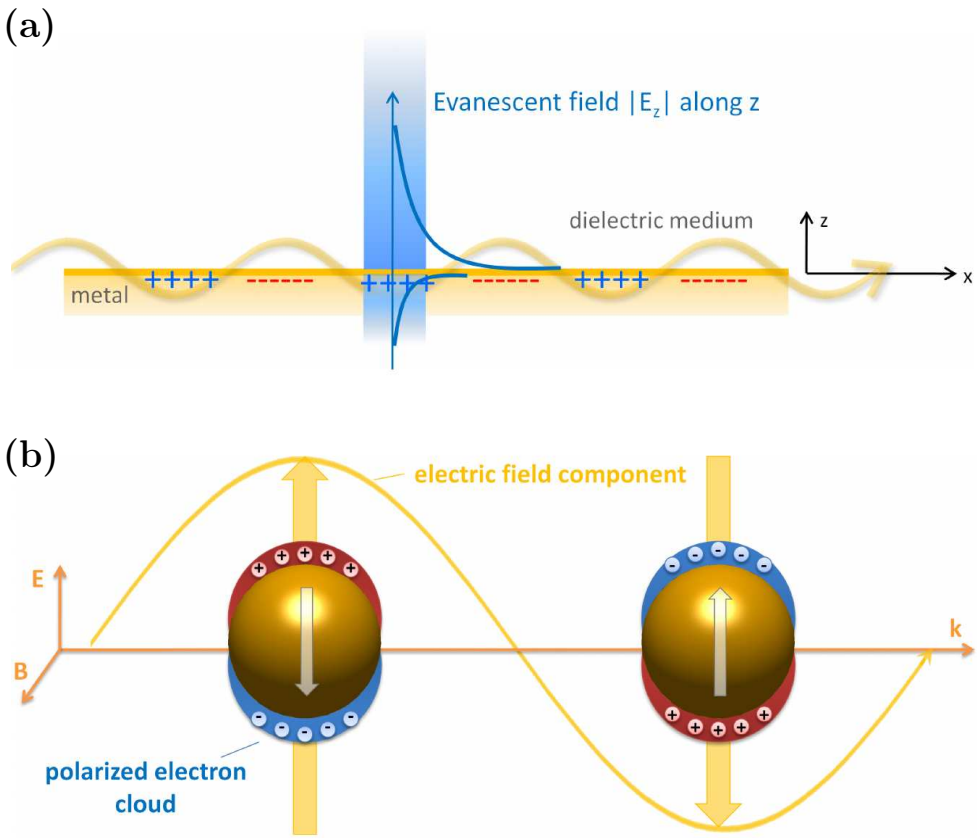

Figure 3: Illustration of **(a)** a propagating surface plasmon and **(b)** a localized surface plasmon.[45]. The arrows represent the dipole moment induced in the particles by the external electric field.

optical response, characterized by the dielectric function $\epsilon(\omega)$ of the material. Thus, no further mention to free-electron motion is needed.[1]

Among the different types of plasmons that can exist in a material, we are particularly interested in the so-called *surface plasmon-polaritons*, that occur in the interface between different materials (normally a metal and a dielectric medium). The polariton denotation comes from the fact the these plasmons are excited when coupled to electromagnetic waves (photons). The term plasmon-polariton thus means that the excitations are mixed plasmon-photon modes.[1] They can be further divided into propagating surface plasmon-polaritons (PSPPs), when the plasmon mode can propagate along the metal-dielectric surface, and localized surface plasmon-polaritons (LSPPs) for plasmons that are confined in a region, producing evanescent waves. Fig. 3(a) shows a PSPP that is confined to the interface (evanescent waves in z direction) but propagates along the surface (x direction). In Fig. 3(b), we have a LSPP example in a metallic nanoparticle; the size of the particle prevents the plasmon mode from propagating and it remains restricted to the small surface of the particle. As we are concerned about plasmons in nanostructures, our focus will be on LSPPs.

2.2 Plasmons in Nanoparticles

In order to understand how plasmons behave in NPs, consider a sphere with radius a and dielectric function $\epsilon(\omega) = \epsilon_R + i\epsilon_I$ inserted in an isotropic and non-absorbing medium whose dielectric function is ϵ_m. Assuming that the sphere is much smaller than the wavelength of the incident light in the surrounding medium (λ_{inc}), the incident electric field at the sphere can be considered as uniform, $\boldsymbol{E}_{inc} = \boldsymbol{E}_0$. This assumption is known as the *quasi-static approximation* (QSA), being also called the electrostatic approximation, or the long-wavelength approximation, or the Rayleigh approximation. The QSA is valid regardless of the particle shape and is normally limited to particle sizes below $\lambda_{inc}/20$.[1]

Within QSA, the problem then becomes a electrostatic problem in which the electrostatic potential can be found by solving the Laplace equation. Therefore, the electric field distribution inside ($\boldsymbol{E}_{in}$) and outside the sphere ($\boldsymbol{E}_{out}$) can be determined, being given by‡

$$\begin{cases} \boldsymbol{E}_{in} = \dfrac{3\epsilon_m}{\epsilon + 2\epsilon_m}\boldsymbol{E}_0, & (2.8) \\ \boldsymbol{E}_{out} = \boldsymbol{E}_0 + \dfrac{3\hat{\boldsymbol{r}}(\hat{\boldsymbol{r}}\cdot\boldsymbol{p}) - \boldsymbol{p}}{4\pi\epsilon_0\epsilon_m r^3}, & (2.9) \end{cases}$$

in which $\boldsymbol{p} = 4\pi\epsilon_0\epsilon_m a^3 \dfrac{\epsilon - \epsilon_m}{\epsilon + 2\epsilon_m}\boldsymbol{E}_0$ is the induced dipole moment inside the sphere. From eq. (2.9), we verify that the outer field is basically the incident field plus the contribution of the dipolar field produced by $\boldsymbol{p}$. Defining the polarizability α such that $\boldsymbol{p} = \epsilon_0\epsilon_m\alpha\boldsymbol{E}_0$, we have that

$$\alpha = 4\pi a^3 \frac{\epsilon - \epsilon_m}{\epsilon + 2\epsilon_m} \tag{2.10}$$

The time dependence of the incident fields can be included by assuming that the particle is small enough for spatial retardation effects be neglected.[2] By this approximation, if $\boldsymbol{E}_{inc}(\boldsymbol{r}, t) = \boldsymbol{E}_0 e^{i\omega t}$ (plane wave), the induced dipole in the sphere now oscillates accordingly, $\boldsymbol{p}(t) = \epsilon_0\epsilon_m\alpha\boldsymbol{E}_0 e^{i\omega t}$. The scattering and absorption cross-sections (CS) can then be calculated by dividing the total radiated power of $\boldsymbol{p}(t)$ and its absorbed power by the incident power density, respectively. Thus,

$$\begin{cases} \sigma_{sca} = \dfrac{k^4}{6\pi}|\alpha|^2 = \dfrac{8\pi}{3}k^4 a^6 \dfrac{(\epsilon_R - \epsilon_m)^2 + \epsilon_I^2}{(\epsilon_R + 2\epsilon_m)^2 + \epsilon_I^2}, & (2.11) \\ \sigma_{abs} = k\,\mathrm{Im}[\alpha] = 4\pi k a^3 \dfrac{3\epsilon_m\epsilon_I}{(\epsilon_R + 2\epsilon_m)^2 + \epsilon_I^2}, & (2.12) \end{cases}$$

with $k = \dfrac{2\pi}{\lambda} = \dfrac{\sqrt{\epsilon_m}}{c}\omega$. These equations show that σ_{sca} scales with a^6 while σ_{abs} scales with a^3. This means that the extiction CS $\sigma_{ext} = \sigma_{sca} + \sigma_{abs}$ is dominated by absorption

‡The details on how to get to these expressions are provided in many textbooks.[1,2,43]

for small NPs and by scattering for larger NPs. This effect is then useful to estimate particle sizes in real samples.[43,46]

As $\epsilon(\omega)$ is a general dielectric function, the equations obtained so far are valid independently of the optical response of the sphere material. For a normal dielectric ($\epsilon(\omega) > 1$) then, no plasmonic resonance is possible; however, for a metal, there is a resonance when $\epsilon_R(\omega) = -2\epsilon_m$. This resonance corresponds to a enhancement peak in the polarizability, eq. (2.10), and in both electric fields, eqs. (2.8) and (2.9). The intensity of this peak is inversely proportional to $\epsilon_I(\omega)$. Indeed, from eq. (2.12), it is evident that the peak around $\epsilon_R(\omega) = -2\epsilon_m$ becomes larger and narrower as $\epsilon_I(\omega)$ decreases. The discussion in Sec. 2.1 about plasmonic resonances becomes now clear. Such resonances are characteristic for metallic NPs and are called *localized surface plasmon resonances* (LSPRs).

For a Drude dielectric function given by eqs. (2.5) and (2.6), we have that this resonance occurs at the frequency

$$\omega_0 = \sqrt{\frac{\omega_p^2}{\epsilon_\infty + 2\epsilon_m} - \gamma^2} \approx \frac{\omega_p}{\sqrt{\epsilon_\infty + 2\epsilon_m}}, \tag{2.13}$$

for the small-damping limit. Note that ω_0 goes towards smaller frequencies (red-shift) as ϵ_m increases, which means that frequency position of the plasmon peak is sensitive to the surrounding medium. This effect indicates that metallic NPs are good for optical sensing based on the refractive index.[2,12]

This model can be generalized for particle shapes other than spheres. However, as this sphere example already provides the fundamental physics of LSPRs in metallic NPs, we will skip the details of such generalizations. Refs. 47 and 48 not only address these details but also discuss other analytical methods for investigations beyond the QSA, such as Mie Theory.

2.3 Oligomers and Hybridization Model

When studying plasmons in agglomerates of NPs (oligomers), it is very convenient to understand the so-called hybridization model.[49–51] This model is pretty much an analogy to the hybridization theory for molecular orbitals. Consider the case of a dimer of nanospheres, the simplest NP cluster possible. Fig. 4 depicts how the hybridization in a dimer works. When the NPs are far enough, they do not interact and their dipolar plasmon modes are threefold degenerated due to their spherical shape, i.e. all modes have the same energy (E_3). As the particles get closer, their dipoles begin to interact and these modes are energetically split (degeneracy break), producing 4 different coupled modes.

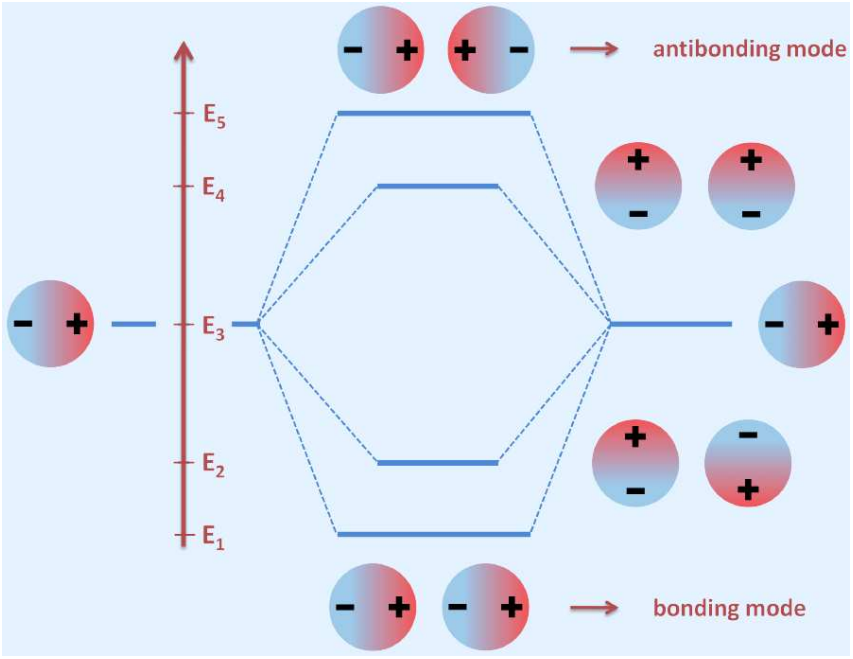

Figure 4: Hybridization model applied to dipolar modes of two nanospheres, i.e., the modes that appear from the combination between the dipoles of each particle.

Two of these modes have resulting energies (E_1 and E_2) lower than the energy of the isolated spheres (E_3), therefore being called *bonding modes*. The other two modes have higher energies (E_4 and E_5) in comparison to E_3 and, consequently, are denominated *antibonding modes*. These energies are related to the excitation energy of the incident light, which means that the incident electromagnetic field must have a smaller (higher) frequency to activate the bonding (antibonding) modes in the dimer. In other words, the bonding (antibonding) modes are redshifted (blueshifted) with respect to the isolated dipole modes. This approach can be easily extended for higher-order modes and larger oligomers.

Plasmonic modes can also be classified according to its total dipole moment. From Fig. 4, we note that the modes labeled by energies E_1 and E_4 have a non-zero dipole moment while modes at E_2 and E_5 have a vanishing net dipole moment. The non-zero dipole modes are called *bright modes* and the modes with null dipole moment are known as *dark modes*. This terminology comes from the fact that dark modes normally cannot be excited by light while bright modes interact strongly with far-field radiation.[§] It is worth emphasizing that this classification in bright or dark modes is not related to whether the mode is bonding or antibonding, as it is possible to find bonding and antibonding modes with bright and dark characteristics (see Fig. 4).

[§]The excitation of dark plasmon modes will be discussed in Sec. 4.1.

3 Methodology

3.1 Finite-Difference Time-Domain (FDTD)

In this thesis, we use the finite-difference time-domain (FDTD) method to simulate the optical response of the noble-metal NP layers. The FDTD method consists basically in solving the full Maxwell's equations by employing finite differences in both space and time. By using second-order central-difference approximation to the space and time partial derivatives, the differential equations become algebraic equations that associate the electromagnetic fields in a former time to the fields in a later time. The method works as a computational experiment, in which the user can set up all the details of the system to be simulated and all the monitors that will capture the electric and magnetic fields as function of space and time (or frequency if a Fourier Transform is applied). With these fields, many other quantities can then be determined, such as transmittance, reflectance and induced charges. In general, the method is very versatile, easy to understand and intuitive to model complex situations, but, depending on the system, it may demand a lot of memory and computational power.

The FDTD method as an algorithm consists essentially in the so-called Yee algorithm, referring to Kane Yee, who first presented this scheme in 1966 [52]. To clearly understand this algorithm, we can apply it to a simple case. Consider a one-dimensional problem, i.e. that all fields vary only along the x direction, and that there are no free charges and currents. Assume also that the electric field has only component along z, $\boldsymbol{E}(\boldsymbol{r},t) = E_z(x,t)\hat{\boldsymbol{z}}$. By the Faraday's law, we have that

$$-\mu\frac{\partial \boldsymbol{H}}{\partial t} = \nabla \times \boldsymbol{E} = -\frac{\partial E_z}{\partial x}\hat{\boldsymbol{y}}, \tag{3.1}$$

which means that only the y component of the magnetic field is time dependent. Thus we will consider that $\boldsymbol{H}(\boldsymbol{r},t) = H_y(x,t)\hat{\boldsymbol{y}}$. For the discretization of the space and time, the following notation can be used:

$$\begin{cases} E_z(x,t) = E_z(m\Delta_x, q\Delta_t) = E_z^q\,[m]\,, \\ H_y(x,t) = H_y(m\Delta_x, q\Delta_t) = H_y^q\,[m]\,, \end{cases} \tag{3.2}$$

in which Δ_x and Δ_t are the discretization steps in space and time. m and q are the indexes that label the spatial position and time of each point in the spatiotemporal grid generated from the discretization. The grid is illustrated in Fig. 5. Although our example considers just one dimension in space, it is actually a 2D problem due to the time dependence.

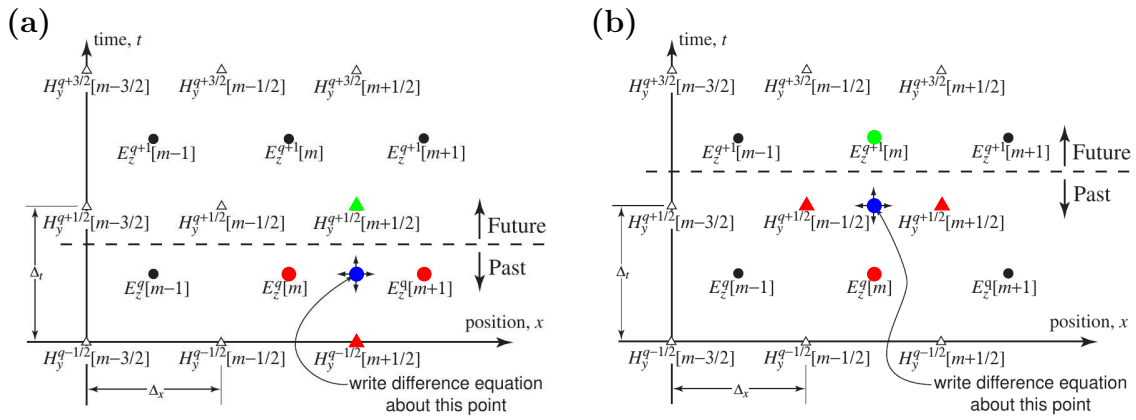

Figure 5: Illustration on how FDTD method works for the simplest case of 1D space. The dashed lines are the lines of the present, that separates past (known) fields and future (unknown) fields. **(b)** represents the same system as **(a)** but at one half temporal step later. The blue circles represent the points where the differential equations are calculated. When solving the equations, the field values at the red points are used to determine the field at a point in a half time step in the future (green points).[53]

The dashed line separates the points where all fields are known (below the line) from the points where the fields still need to be calculated (above the line). We can think of this line as representative for the present moment, such that the past is considered below the line while the future lies above the line. Note that the electric and the magnetic fields are discretized differently. There is an offset of $\frac{\Delta_x}{2}$ in space and $\frac{\Delta_t}{2}$ in time between the grids where the electric field (circles) and magnetic field (triangles) are defined. These offsets make possible the easy implementation of the discretization in the Maxwell's differential equations.

By applying the Faraday's law at the space-time point $((m+\frac{1}{2})\Delta_x, q\Delta_t)$, the blue circle in Fig. 5(a), the following equation can be written

$$H_y^{q+\frac{1}{2}}\left[m+\frac{1}{2}\right] = H_y^{q-\frac{1}{2}}\left[m+\frac{1}{2}\right] + \frac{\Delta_t}{\mu\Delta_x}\left(E_z^q\left[m+1\right] - E_z^q\left[m\right]\right). \tag{3.3}$$

By repeating this calculation to all other points at the border of the dashed line, all magnetic fields at time $(q+\frac{1}{2})\Delta_t$ become known and the line of the present advances a half time step $(\frac{\Delta_t}{2})$ into the future, Fig. 5(b). Now we can apply the Ampere's law at the space-time point $(m\Delta_x, (q+\frac{1}{2})\Delta_t)$, the blue circle in Fig. 5(b), and find that

$$E_z^{q+1}\left[m\right] = E_z^q\left[m\right] + \frac{\Delta_t}{\epsilon\Delta_x}\left(H_y^{q+\frac{1}{2}}\left[m+\frac{1}{2}\right] - H_y^{q+\frac{1}{2}}\left[m-\frac{1}{2}\right]\right). \tag{3.4}$$

Similarly to eq. (3.3), all other electric field values at time $(q+1)\Delta_t$ can be determined by recursively applying eq. (3.4) and the line of the present can move further another half time step. Afterward, the situation becomes similar to that depicted in Fig. 5(a) and

the calculation process can be repeated indefinitely or until a cutoff parameter reaches a threshold value. Equations (3.3) and (3.4) are known as *Update Equations* since they essentially use past field values, the red points in Fig. 5(a) and (b), to update the electric and magnetic fields at a later time instant (green points). In general terms, if the initial conditions of a electromagnetic system are given, we can find the resulting fields at any later time with these equations.

This example addresses the main points of the method. With this digression, we hope to have clarified the basic ideas behind the FDTD method and how it is implemented. For further details about the FDTD method, the book from Schneider[53] provides not only the generalizations for more complex systems but also discusses computer implementation of the method.

All simulations in this thesis were performed with Lumerical FDTD Solutions, a commercial software package. The monolayers were considered as two-dimensional crystal lattices and simulated by defining a square unit cell and using periodic boundary conditions. The bi- and fewlayers were implemented by adding more NPs to the unit cell such that the NPs arrangement determines the layers stacking (align and hcp). Mesh-override regions of 0.25 nm were used for systems with particle diameters below 15 nm and gap sizes below 3 nm while, for larger diameters and gaps, an override mesh size of 1 nm was used. Two power monitors were included; one behind the layers to capture the transmittance T, and another one behind the source for the calculation of the reflectance R. The absorbance A was later computed as $A = 1-T-R$. A plane-wave source was used for the layers simulations while a total-field scattered-field source was used to calculate the cross-section of nanoparticle dimers. The gold and silver dielectric functions were implemented by fitting the experimental data provided by Johnson and Christy[44] and by Palik[54], respectively. The mesh sizes were varied to test the convergence and assure the accuracy of the simulated results. The polarization density $\boldsymbol{P}$ was calculated from the simulation data for the electrical current density* $\boldsymbol{J}$ by using the relation $\boldsymbol{J} = \frac{d\boldsymbol{P}}{dt}$ and assuming a harmonic time dependence. The spatial average over the unit cell region of each layer ($< \boldsymbol{P} >$) was then computed in order to observe just the mean behavior of the polarization.

We consider layers of close-packed metallic nanospheres of equal size, as illustrated in Fig. 6 for the bilayer. In all simulations, a linearly polarized plane wave with propagation normal to the layers was used as the light source. The polarization direction was set as the x direction, although any other polarization direction would lead to the same spectra because of the hexagonal symmetry of the nanoparticle lattice. In Fig. 23, an amorphous

*Lumerical has a monitor that calculates the current density from the electric field values by using the relation $\boldsymbol{J} = -i\omega(\epsilon_{material} - \epsilon_0)\boldsymbol{E}$, in which $\epsilon_{material}$ is the effective permittivity at every point inside the simulation area.

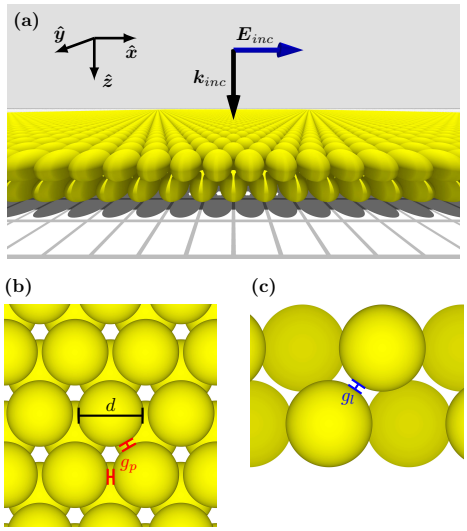

Figure 6: Example of a bilayer of gold nanospheres investigated in this study in three different views: **(a)** perspective view, **(b)** top view (plane xy) and **(c)** side view (plane yz). $\boldsymbol{k}_{inc}$ and $\boldsymbol{E}_{inc}$ indicate the propagation and polarization directions of the incident light, respectively. In **(b)** and **(c)**, the particles diameter (d), the gap between neighboring particles in the layers (g_p) and the gap between the layers (g_l) is indicated.[42]

carbon film with 10 nm thickness was included below the layers as in the experiments. The dielectric function of the amorphous carbon was taken from the experimental data of Larruquert *et al.*[55]. In Sec. 4.7, the layers were placed on top of a 200 nm thick gold slab. For further details on the simulation settings, the table 1 shows the relevant parameters used in all simulations presented in this thesis.

Throughout the thesis, we will use the following notation regarding the layers structural parameters: d is the particles diameter, g_p is the the edge-to-edge spacing (gap) between particles within one layer and g_l is the gap between the layers; see Figs. 6(b) and (c). The variable g without subscript is used when g_p and g_l have equal values and are simultaneously changed ($g \equiv g_p = g_l$). Regarding the spectral features of the plasmon modes, we will denote their excitation energy (peak position) as E and their full width at half maximum (FWHM) as γ.

Parameter	Value
FDTD Simulation Region	
Background Index (n)	$n = 1$ in Secs. 4.2 and 4.3 and $n = 1.4$ in Secs. 4.4, 4.5, 4.6 and 4.7
Geometry: xy Plane	Size of the Unit Cell
Geometry: z Axis	600 nm+(Thickness of the Whole System)
Simulation Time (fs)	500
Simulation Temperature (K)	300
Mesh type and refinement	Auto Non-Uniform, Conformal Variant 0
Mesh Accuracy	Level 5
Minimum Mesh Size	0.25 nm
Time step	dt stability factor 0.99
Boundary Conditions	
x and y Axis	Periodic with Symmetry Planes when possible.
z Axis	Perfect Matching Layer of type stretched coordinate PML with steep angle profile and 12 Layers
Early Shutoff	$1e-05$
Mesh Override Region	
Mesh Size	0.25 nm for $d \leq 15$ nm and $g \leq 3$ nm 1 nm otherwise
Geometry	Covering All NP Layers Volume
Light Source	Bloch/Periodic Plane Wave
Amplitude	1
Injection Axis and Direction	z-axis and Backward
Phase and All Angles	0
Geometry	Spanning the xy Plane at 150 nm above the NP Layers.
Frequency domain power monitors	
Transmitance	2D Z-normal Monitor at the lowermost border of the FDTD Simulation Region
Reflectance	2D Z-normal Monitor at upppermost border of the FDTD Simulation Region
Current Charge Density Monitors	One Monitor per Layer. Average Current calculated via Script
NP Layers	2D Lattice spanning the xy Plane. All spheres with the same diameter d.
Amorphous Carbon Film	Spanning the xy Plane with 10 nm Thickness. Placed right below the layers.
Gold Slab	Spanning the xy Plane with 200 nm Thickness.
SiO_2 Film	Spanning the xy Plane with 100 nm Thickness.
Location	Between the NP Layers and the Gold Slab.
Material parameters	All with 15 coefficients
Au (Gold) Johnson and Christy	0.01 fit tolerance and 30 imaginary weight
Ag (Silver) Palik (0-2μm)	0.1 fit tolerance and 10 imaginary weight

Table 1: Summary of values for the important parameters used in the simulation settings.

4 Results and Discussions

This investigation was a result of intense collaborations. I've performed all the simulations with FDTD and provide the theoretical understanding with the crucial help of Niclas S. Mueller, who also performed the microabsorbance measurements. Florian Schulz and Holger Lange were responsible for synthesizing the mono-, bi-, tri- and few layers colloids made of nanospheres. They also performed the pump-probe measurements that gave better understanding of these materials as hot-electron generators. In the following chapter, there are excerpts from Ref. 42.

4.1 Dark Plasmon Excitation

Dark plasmons (as discussed in Sec. 2.3) normally do not interact with far-field radiation. However, various approaches have been proposed (and partly demonstrated) for their excitation, such as breaking the symmetry of a system to turn the dark plasmon slightly bright[32–34,56], using light sources with spatial polarization profiles[38–40,57] and using localized emitters to excite the dark plasmons through evanescent fields[35,36]. Dark plasmons can also be observed indirectly through their interaction with a bright mode, which generates asymmetric line shapes called Fano resonances[31,41]. Although these methods are very useful for studying dark plasmons, they demand either complicated techniques for synthesizing the plasmonic nanostructure or sophisticated laser beam profiles, which makes them very expensive and not suitable for large-scale applications.[23]

We will show that the noble-metal NP layers allow dark plasmon excitations with linearly polarized light at normal incidence. The principle behind this excitation is the field retardation. To understand the details of this mechanism, consider a dimer of gold nanodisks. As we discussed in Sec. 2.3, the hybridization model predicts that the dimer has four dipolar plasmon modes, illustrated in Fig. 7(a). These modes arise from the combination of the dipolar modes of the single disks and they are labeled according to their representation in the point group D_{2h}*. B_{3u} and B_{2u} are the bright modes, whose NP dipoles are parallel and aligned to the x (dimer axis) and y directions, respectively, see the coordinate system in Fig. 7(b).[60]. A_{1g} and B_{1g} are then the dark modes. They are respective anti-parallel dipole configuration correspondent to B_{3u} (x axis) and B_{2u} (y axis).

Using only plane linear electromagnetic wave as the incident light, it is clear that

*For more information about group theory representations and their physical meaning, please refer to the books from Hamermesh[58] and Dresselhaus *et al.*[59].

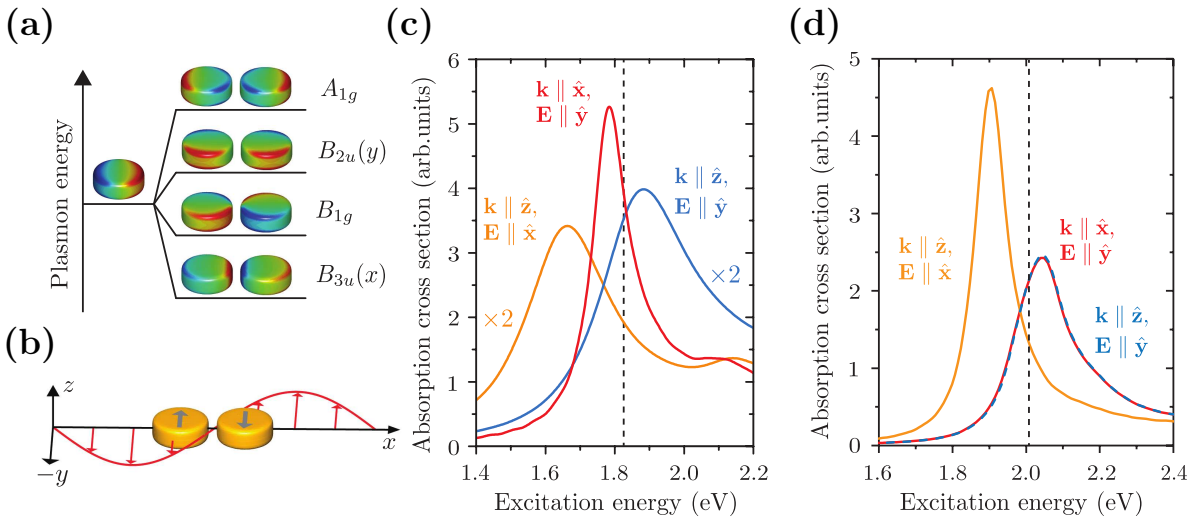

Figure 7: Dark plasmon excitation in dimers via field retardation. **(a)** Hybridization scheme of the dipolar plasmon modes of a nanodisk dimer. The colormap represents the surface charges, in which red (blue) color means positive (negative) charges. It was calculated with boundary-elements method (MNPBEM Toolbox)[61]. **(b)** Illustration on how the B_{1g} dark mode can be excited with side illumination. The dipole moments at each disk are indicated by the gray arrows while the red line and arrows represent the electric field distribution at specific times. **(c)** Simulated absorption cross-section (CS) of a gold nanodisk dimer with 100 nm disk diameter, 20 nm disk height and 20 nm gap. The dimer is surrounded by a medium with refractive index $n = 1.33$ (water) and the calculations were taken for various light propagation directions and polarization. The black dashed line indicates the energy of the dipolar plasmon mode of one single nanodisk of the dimer. **(d)** Simulated absorption cross-section (CS) of a dimer similar to **(c)** but whose dimensions are 5 times smaller (20 nm disk diameter, 4 nm disk height, 4 nm gap). The black dashed line indicates the energy of the dipolar plasmon mode of one single nanodisk of the dimer. Reprinted with permission from Ref 23.

both bright modes can be excited with light propagating along the z axis. Mode B_{3u} is excited with light polarized along the x axis while, for B_{2u} excitation, the light polarization needs to be along the y axis. FDTD simulations demonstrate this analysis through the calculation of the dimer absorption cross-section. Fig. 7(c) shows the CS for a nanodisk dimer with diameter 100 nm, height 20 nm and gap 20 nm between the disks. The whole system is immersed in water ($n = 1.33$) and different propagations ($\hat{\boldsymbol{k}}$) and polarizations ($\hat{\boldsymbol{E}}$) for the incoming wave were considered. The orange curve ($\hat{\boldsymbol{k}} = \hat{\boldsymbol{z}}$ and $\hat{\boldsymbol{E}} = \hat{\boldsymbol{x}}$) shows the peak related to the bright mode $B_{3u}(x)$ at 1.66 eV while the blue line ($\hat{\boldsymbol{k}} = \hat{\boldsymbol{z}}$ and $\hat{\boldsymbol{E}} = \hat{\boldsymbol{y}}$) shows the peak for the bright mode $B_{2u}(y)$ at 1.88 eV. In both cases, no dark mode is excited. However, when light comes along the x axis ($\hat{\boldsymbol{k}} = \hat{\boldsymbol{x}}$) with polarization along y ($\hat{\boldsymbol{E}} = \hat{\boldsymbol{y}}$), a peak related the dark mode B_{1g} is observed at 1.78 eV (red curve). This situation corresponds to the illustration shown in Fig. 7(b). The energy distribution of the peaks are in total agreement with the dimer energy splitting discussed in Sec. 2.3. From the curves, we observe that the B_{1g} linewidth is roughly two times narrower than the linewidth of the bright modes.

As mentioned before, the dark plasmon excitation is possible due to field retardation effects that begins to be relevant for larger particles compared to the wavelength of the incoming light.[26,37] Common group theory analysis does not apply in this case because it normally consider the light wavelength infinitely large compared to the dimensions of the scatterers. Although the selection rules that arise from this approximation are valid for atoms and small molecules, they cannot be used to analyze larger nanostructures such as the considered nanodisk dimer. Therefore, plasmon modes that were forbidden for small systems may now be excited, which is exactly the case of mode B_{1g}. Due to the dimer size, there are moments when the incident electromagnetic wave has a node exactly at the inversion center of the dimer, meaning that the electric fields at each disk, red line and arrows in Fig. 7(b), are in opposite phase and induces a antisymmetric dipole configuration in the dimer (gray arrows). This behavior should be maximized when the distance between the centers of each disk is equal to $\frac{\lambda_{inc}}{2}$, where λ_{inc} is the wavelength of the incident light.

The $B_{2u}(y)$ peak at 1.88 eV is also expected to appear when $\hat{\boldsymbol{k}} = \hat{\boldsymbol{x}}$ and $\hat{\boldsymbol{E}} = \hat{\boldsymbol{y}}$, the red curve of Fig. 7(c). However, this peak is absent in the spectrum since it is suppressed by the B_{1g} peak. It turns out that the dark mode is dominant for this illumination scheme when the dimer size is sufficiently large for the retardation effects to become relevant; note that the orange and blue curves in Fig. 7(c) are the absorption CS multiplied by a factor of 2. By performing the same calculations for a dimer whose dimensions are $\frac{1}{5}$ of the original dimer (the distance between the centers equals to 24 nm), the dark B_{1g} plasmon peak no longer appears for the side illumination and we have only the bright $B_{2u}(y)$ mode being excited, resulting in the same spectrum for $\hat{\boldsymbol{k}} = \hat{\boldsymbol{z}}$ and $\hat{\boldsymbol{E}} = \hat{\boldsymbol{y}}$, see Fig. 7(d). These simulations confirm the importance of the field retardation to the excitation of the B_{1g} dark mode.

Although the dimer example is useful to understand the dark mode excitation mechanism, it is not experimentally feasible since it would require shining light along the surface of the substrate in which the dimer is deposited. One workaround for this issue is to put one particle at the top of another and this approach was done by using metal-insulator-metal (MIM) nanodisks[26–30,37,62–64]. An alternative to this approach is to use the NP layers, in which we can show that the bilayers produce the same effect as the dimer case.[23]

4.2 Nanoparticle Monolayer

Before studying the NP bilayers, let's begin our investigation by analyzing the simplest case, i.e., a monolayer of hexagonally packed metallic nanospheres. In this section and

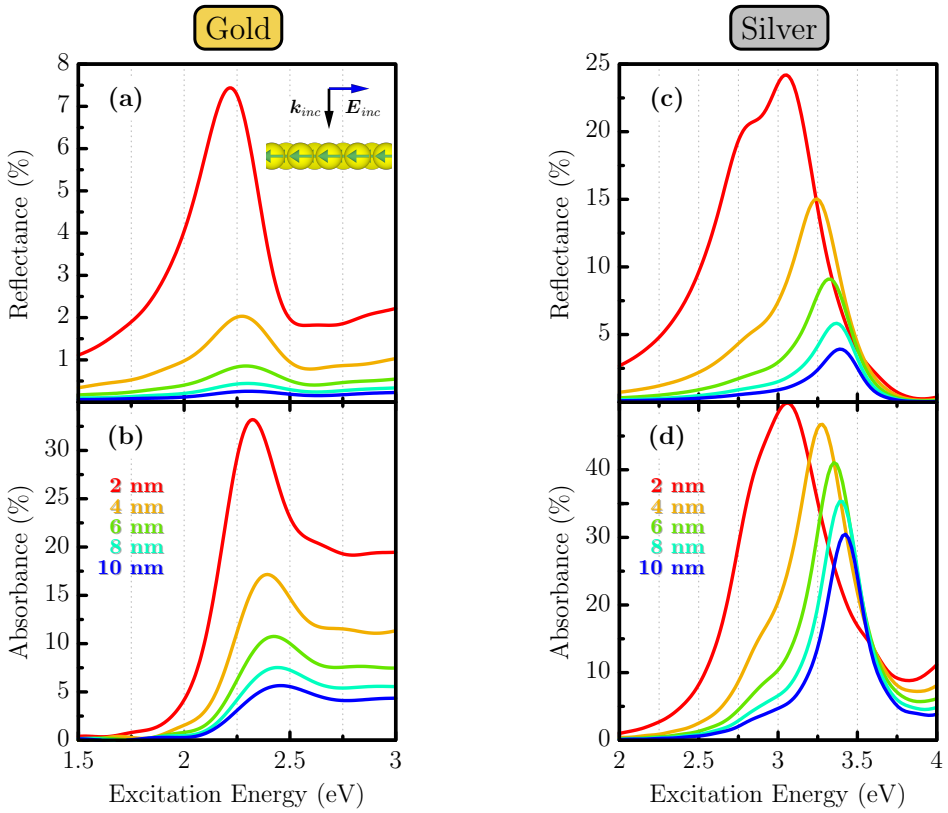

Figure 8: Reflectance and absorbance spectra calculated for hexagonal monolayers of nanospheres with diameter $d = 10$ nm. The spectra for different gap sizes (g) are shown. The left panels present the **(a)** reflectance and **(b)** absorbance spectra for gold NPs while the right panels show the **(c)** reflectance and **(d)** absorbance spectra for silver NPs.[42]

in the following (Sec. 4.3), we considered vacuum as the surrounding medium ($n = 1$). Figure 8 shows the absorbance and reflectance spectra of a single layer of nanospheres with $d = 10$ nm. Its optical response is polarization insensitive as the monolayers have a hexagonal symmetry (Point Group D_{6h})[60]. Spectra for both gold and silver monolayers are presented and the distinct curves in each panel indicate the influence of the gap between the particles (g). For gold, a plasmon mode is excited around 2.35 eV in all the cases and increases in intensity as g decreases. This mode corresponds to the dipole-active mode in which all NPs have parallel dipole moments of similar magnitude (see inset of Fig. 8(a)). The absorbance spectrum is dominant over reflectance, because small spheres are poor scatterers of light as they do not have a large amount of material to prevent light from being transmitted. There is a slight redshift that stems from the increased coupling between the particles as g is reduced. For silver monolayers, we observed a very similar response (see Fig. 8(c) and (d)). The main differences are that the plasmon mode redshift is more prominent and the reflectance and absorbance peaks are more intense in comparison to gold. Similar shifts has been observed previously in the optical response of nanosphere colloids[65] and metallic NP oligomers, such as spherical and elliptical dimers[14,66–73], nanorod dimers and bowtie antennas[36].

To get a deeper understanding of the spectra of the NP monolayers, we draw a comparison to the simple case of a dimer of spheres illuminated from the top. Figure 9 exhibits the absorption and scattering CSs of a dimer of particles with $d = 10$ nm (same d as in Fig. 8). Simulations for light polarization along and perpendicular to the dimer axis are presented in order to account for the different angles between the incident light polarization and each of the particle pairs in the layer. As expected, there is a redshift with decreasing g for light polarization along the dimer axis, Fig. 9(a), and a blueshift for perpendicular polarization, Fig. 9(b). The shifts are overall small due to the small size of the NPs[14,66,68,69,73]. For better visualization, the zoomed spectral range of the scattering CS spectra are shown as insets in Figs. 9(a) and (b). The parallel polarization causes a bonding plasmon mode in the structure, i.e., the induced dipole configuration makes the particles to have an attractive interaction, see inset in Fig. 9(c). On the other hand, the perpendicular polarization excites an antibonding mode (repulsive interaction between the particles), as in the inset of Fig. 9(d). As g is reduced, the bonding (antibonding) coupling increases, which causes the mode to shift towards lower (higher) energies, i.e., a redshift (blueshift). The dipoles of bonding mode are oriented parallel to the dimer axis while the dipoles of the antibonding mode are perpendicular to it. This orientation difference indicates that the bonding coupling is more intense than the antibonding coupling, an effect that is similar to the observed difference in coupling strength for σ and π bonds in molecules. It is expected then that the bonding mode is subjected to a redshift that is larger in magnitude than the blueshift of the antibonding mode.

Back to the monolayer of NPs, there are pairs of particles with a dipole configuration similar to each of the dimer modes shown in Fig. 9 (bonding and antibonding modes) while others have a dipole configuration that is a combination of these two modes depending on their orientation (a more detailed description of this coupling will be given further on). Therefore, the fact that the monolayer absorbance shows a redshift with decreasing g similarly to exciting the dimer with polarization along its axis means that the overall bonding contribution of the particles affects the energy stronger than the total antibonding contribution.

Let us now evaluate how the particles diameter d affects their optical properties. In Fig. 10 the absorbance and reflectance spectra of gold monolayers are displayed for various d using a gap size $g = 2$ nm.[†] The plasmon mode observed in Fig. 8 is also excited in larger spheres. As d increases, an absorbance tail above 2.25 eV rises and overlaps the plasmonic peak. This behavior stems from the increase of the interband transitions of gold, caused by the increasing amount of material, in the case of the larger spheres. As LSPRs are surface effects and the interband transitions are related to the NP volume[2,74],

[†]As we did not expect much difference for silver monolayers, we decided not to perfom simulations on diameter dependence for them.

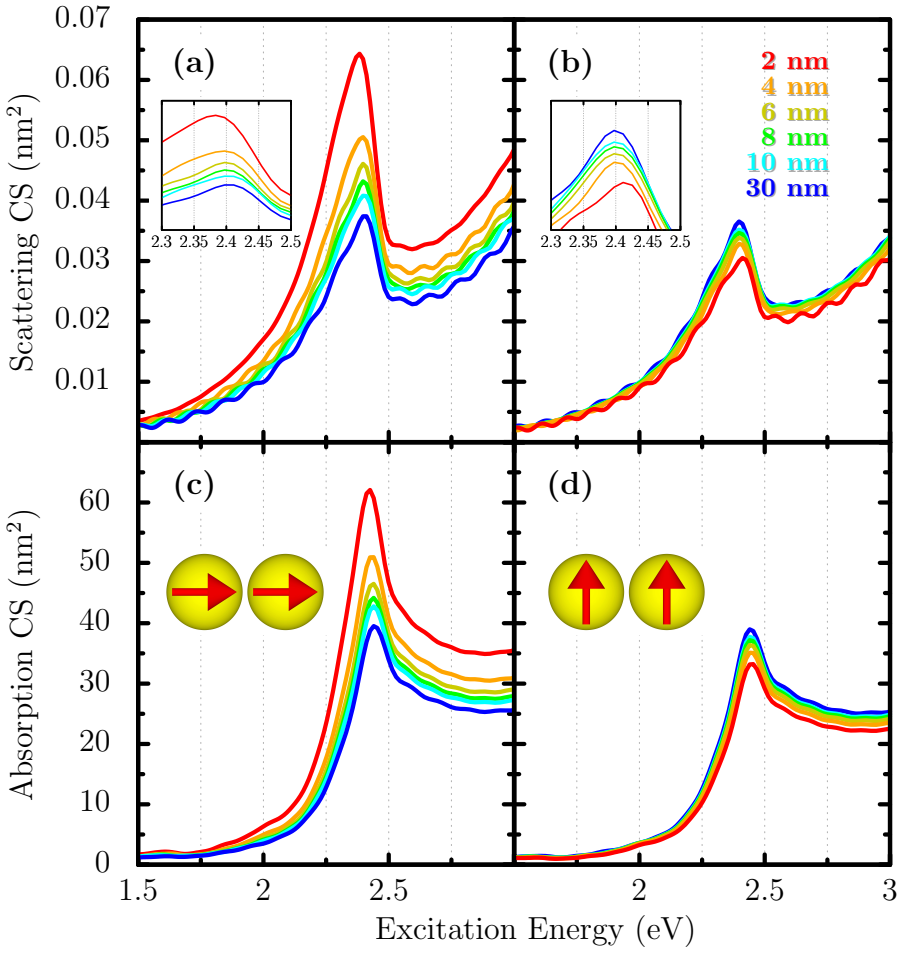

Figure 9: Absorption and scattering CSs of a dimer of nanospheres with $d = 10$ nm as function of the gap size between the NPs. The left panels show the **(a)** scattering and **(c)** absorption CS for the light polarization along the dimer axis while the right panels show the **(b)** scattering and **(d)** absorption CS for the polarization perpendicular to it. The insets in **(a)** and **(b)** show the zoomed spectral range around the resonance peaks and, in **(c)** and **(d)**, the insets indicate the dipole configuration of each particle for the different polarizations.[42]

the damping of the plasmon mode is indeed expected due to the decrease of the NPs surface-to-volume ratio with increasing d. The volume increase is also responsible for the overall enhancement in the reflectance spectra that goes from less than 10% for $d = 10$ nm to a peak of almost 90% for $d = 60$ nm, see Fig. 10(a). For the absorbance in Fig. 10(b) we note that the spectrum at $d = 20$ nm is slightly out of the trend with respect to the larger diameters, indicating that the plasmon mode is still not completely damped away by the interband transitions for 20 nm diameter particles.

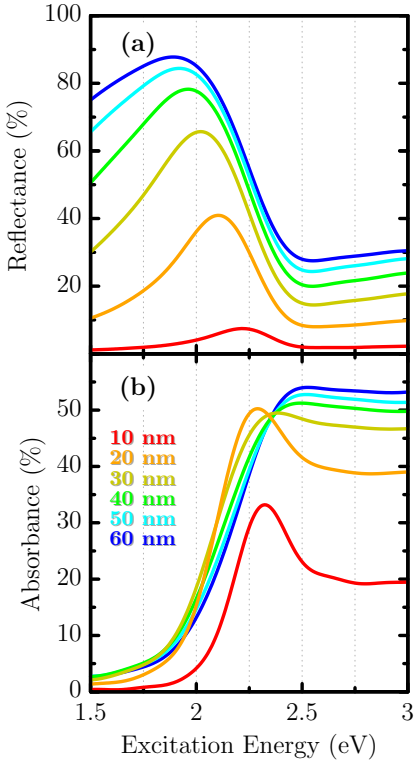

Figure 10: Diameter dependence of the **(a)** reflectance and **(b)** absorbance for gold nanosphere monolayers with $g = 2$ nm.[42]

4.3 Nanoparticle Bilayer

Figure 11(a) shows the absorbance and reflectance for a gold bilayer of nanospheres with $d = 50$ nm and $g = 2$ nm. A prominent absorbance peak emerges at $E_D^{(Au)} = 1.82$ eV together with a reflectance dip at 1.79 eV. The peak has a FWHM of $\gamma_D^{(Au)} = 146$ meV. The dipole-active plasmonic mode observed for the monolayer structures is no longer visible in Fig. 11(a) (Compare with Fig. 8). In the bilayers, the interband transitions of gold are further increased in comparison to the monolayers due to their larger amount of gold, similarly to the effect observed for the monolayers with larger NPs. Therefore, the dipole-active mode is completely damped. From this section on, the dipole-active mode will be labeled as B (bright) while the new mode related to the peak at $E_D^{(Au)}$ will be labeled as D (dark).

A very similar optical response was found for bilayers of silver NPs with an absorbance peak at $E_D^{(Ag)} = 1.97$ eV and a reflectance dip at 1.93 eV. The plasmon mode B is observed as an absorbance peak and a reflectance dip around $E_B^{(Ag)} = 3.30$ eV. This peak is expected because the interband transitions of silver occur at energies larger than 3.8 eV[74], which means that less damping should occur to this plasmonic mode in silver in comparison to gold. Regarding the modes linewidth, the peak at $E_B^{(Ag)}$ has a FWHM of $\gamma_B^{(Ag)} = 830$ meV, whereas the peak at $E_D^{(Ag)}$ has $\gamma_D^{(Ag)} = 217$ meV, i.e., it is almost four times narrower (see

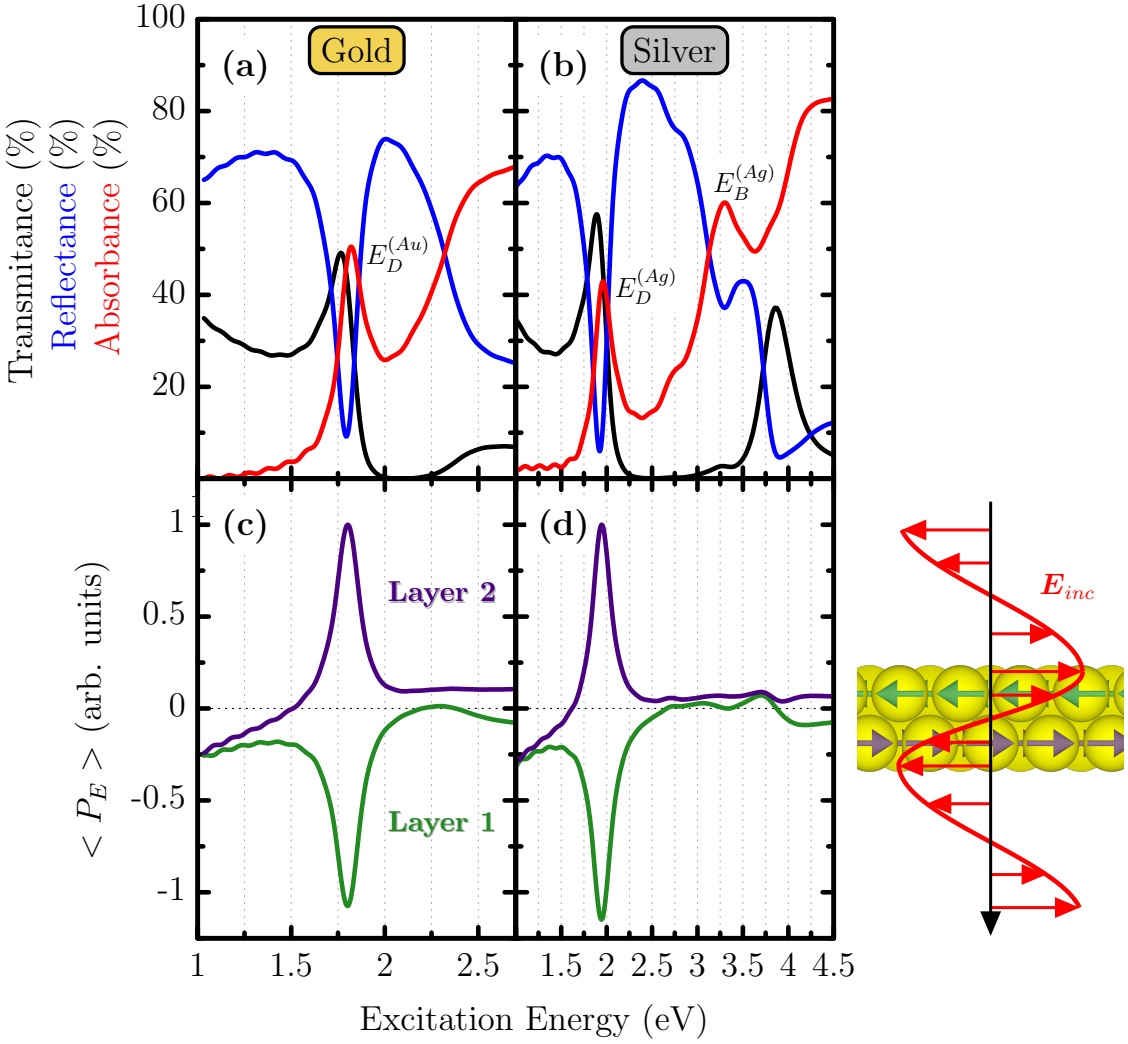

Figure 11: Transmittance (black), reflectance (blue) and absorbance (red) spectra of a bilayer system of **(a)** gold and **(b)** silver NPs ($d = 50$ nm, $g = 2$ nm, hcp stacking). The mean polarization density $< P_E >$ in each layer for **(c)** gold and **(d)** silver as function of the excitation energy is also shown. The subscript E means we are considering the component of $< \boldsymbol{P} >$ that is parallel to the incident electric field $\boldsymbol{E}_{inc}$ (all other components of $< \boldsymbol{P} >$ are null). The inset shows the dipole configuration of the bilayer when the mode D is excited as well as how the excitation mechanism works.[42]

Fig. 13).

To identify the plasmon modes that are being excited, we investigate the charge distribution in the NPs of each layer. We calculate the mean polarization density $< P_E >$ of each layer as a function of the excitation energy (Figs. 11c and d). A peak in both layers is observed at $E_D^{(Au)}$, but the sign of $< P_E >$ is opposite in the two layers. This indicates that the associated absorbance peak and reflectance dip are due to the excitation of a plasmon mode with anti-parallel dipole moments between the two layers. The net dipole moment of the bilayer vanishes, which means that this is a dark plasmon mode[23,56]. Dark plasmons have become more relevant recently since they exhibit little or no radiative

damping and, consequently, longer lifetimes and narrower resonances compared to bright plasmons[26,38,57,75]. This expectation agrees nicely with the remarkable difference between $\gamma_D^{(Ag)}$ and $\gamma_B^{(Ag)}$ in the bilayers.

This dark interlayer plasmon excitation is explained by field retardation, as discussed in Sec. 4.1. Although the particles ($d = 50$ nm) are approximately a tenth of the wavelength of the incident light ($\lambda_{inc} \in [500\text{ nm}, 1000\text{ nm}]$), the bilayer is more than 100 nm thick and the quasi-static approximation is no longer valid. At specific times, the incident electric field points in opposite directions in the two layers, inducing anti-parallel dipole moments in the top and bottom layer. Also the activation of the dark mode is facilitated by the large refractive index of the NP layers, which shrinks the internal wavelength of light inside the metafilm[76], see inset of Fig. 11.

The dark mode is observed in both bilayers of gold, Fig. 11(a), and silver NPs, Fig. 11(b). The dark plasmon in silver NP layers occurs at larger energies than for gold and should even remain in the visible range when the NPs are embedded in a surrounding medium with larger refractive index. For silver, the bright mode at $E_B^{(Ag)}$ can also be studied. Although there is no corresponding peak in the polarization at this energy region, $< P_E >$ has the same sign in both layers, indicating that this mode is bright with the net dipole of each layer pointing in the same direction. It is worth emphasizing that the possibility of activating a dark mode with linearly polarized light makes it much easier to use such dark excitations for applications such as SERS.

4.3.1 Diameter Dependence

In the following, we will evaluate the influence of the structural parameters on the plasmon resonances of the bilayers, beginning with particles sizes. In Figs. 12(a) and (b), the absorbance and reflectance spectra for gold bilayer systems with different d are presented. The mode D is excited for particles with $d \geq 30$ nm. For $d < 30$ nm, the retardation effect is weaker and the system gets closer to the quasi-static limit, making it more difficult to excite D. This observation confirms that the common group theory analysis is no longer valid for particles larger than a certain size (30 nm in this case). We note a redshift in $E_D^{(Au)}$ with increasing d, which stems from the fact that the amount of material per unit volume increases, making the coupling between both layers stronger. The anti-parallel dipole configuration of D corresponds to a bonding configuration. Therefore, stronger coupling decreases the mode energy, i.e., a redshift. Similar shifts were observed in MIM nanodisk arrays when changing disk size[26,27]. There is also a slight increase in $\gamma_D^{(Au)}$, which stems from the increase in radiative damping. However, the peak integrated area is not significantly affected by the peak broadening, since a proportional decrease in the peaks height is also observed (see Fig. 14(b)). The

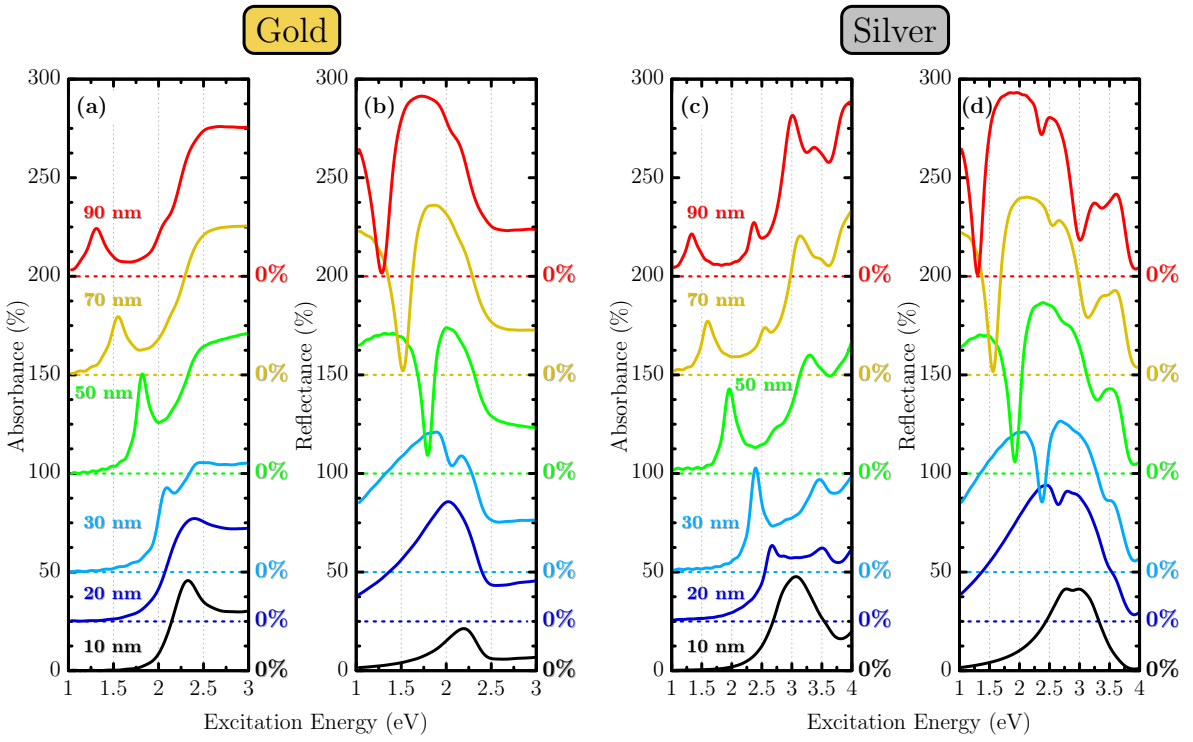

Figure 12: Simulated absorbance and reflectance spectra for different nanosphere diameters with $g = 2$ nm. The color dashed lines indicate the offset of each spectrum. The left panels show the **(a)** absorbance and **(b)** reflectance spectra for gold while the right panels display the **(c)** absorbance and **(d)** reflectance spectra for silver. In both gold and silver, the pronounced absorbance peak related to mode D is strongly redshifted with increasing d followed by its respective reflectance dip.[42]

bright mode is well pronounced for particles with $d < 20$ nm but gets damped by the interband transitions for $d > 30$ nm. The results for silver are shown in Figs. 12(c) and (d). Similarly to gold, $E_D^{(Ag)}$ also goes towards smaller energies when d increases. The mode B shows a weak redshift for larger d and an increase in absorbance intensity. In addition, as the interband transitions get far away on the energy scale, higher-order modes, such as quadrupoles and hexapoles, are also excited for $d \geq 50$ nm.

To provide a relation between d and the plasmon energy and lifetime, the absorbance spectra were fitted by

$$A(\omega) = \alpha F(\omega) + \sum_{j=1}^{n} \frac{I_j \gamma_j^2}{4(\hbar\omega - E_j)^2 + \gamma_j^2}, \tag{4.1}$$

where $\hbar\omega \equiv E_{exc}$ is the excitation energy, n is the number of plasmon modes, I_j is the intensity, E_j is the spectral position and γ_j is the FWHM of the j-th plasmon mode. For gold, $F(\omega)$ is the characteristic absorbance $A_0^{(Au)}(\omega)$ of a gold thin film[77,78], in which we considered the dielectric function of gold calculated by the Lorentz-Drude model[79], while for silver, $F(\omega)$ is a step-like (sigmoid) function that mimics the absorbance spectrum of

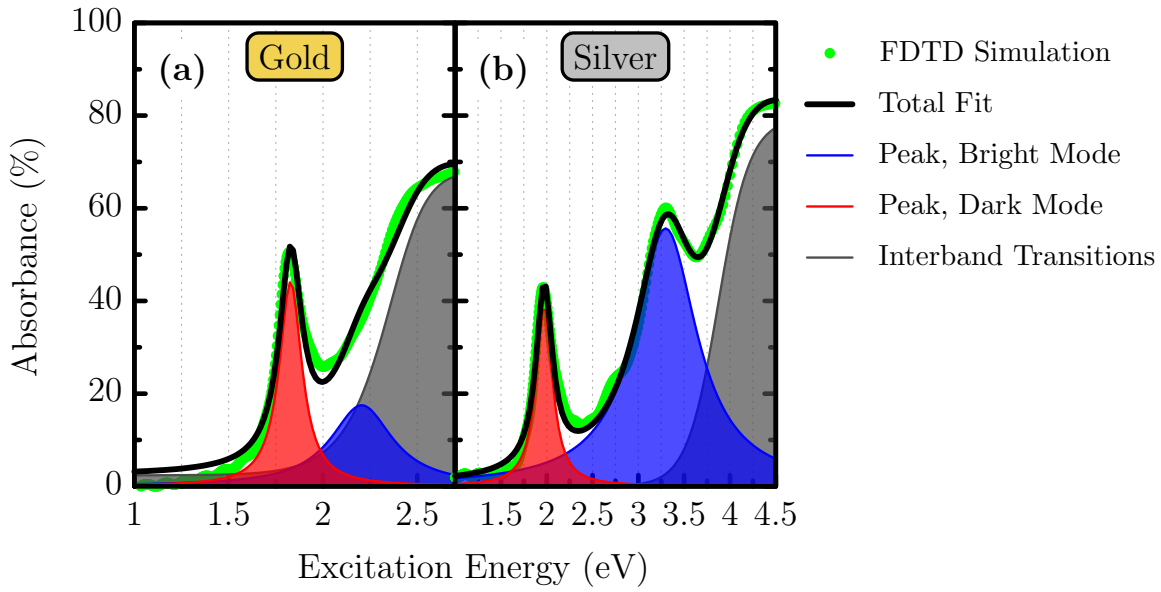

Figure 13: Absorbance spectra of the bilayers (green curve) in which $d = 50$ nm and $g = 2$ nm, i.e, the same systems as in Fig. 11. The spectra are fitted with equation (4.1) (the black curve), in which two Lorentzian peaks were used. In both panels, the red shaded curve corresponds to the peak of the dark plasmon mode while the blue shaded curve corresponds to the peak of the bright plasmon mode. For gold, the dark mode Lorentzian peak is centered at 1.82 eV and has a FWHM of 146 meV while the bright mode peak is at 2.21 eV and has a FWHM of 396 meV. For silver, the Lorentzian peak of the dark mode is at 1.97 eV and has a FWHM of 217 meV while the bright mode peak is centered at 3.30 eV and has a FWHM of 830 meV. The grey line and area represent the $\alpha F(\omega)$ term in equation (4.1), which is the term that takes into account the interband transitions of **(a)** gold and **(b)** silver.[42]

a silver thin film[77,78,80]. $F(\omega)$ is included in order to take the interband transitions into account in the fittings and α is the fitting parameter that accounts for the intensity of these transitions in the material. Fig. 13 shows the fitted curves of the absorbance spectra of Fig. 11 together with the corresponding curves of each term of the eq. (4.1). All sets of parameter values used to fit each curve with Eq. (4.1) are provided in table 2 at the end of this chapter.

In Fig. 14(a), we plot the peak positions and widths of the spectra in Fig. 12(a) as a function of particle diameter. As for $d < 30$ nm only the bright mode is present in the gold spectra, there are no results for the dark mode at this range of diameters. As already mentioned, $E_D^{(Au)}$ shifts to smaller energies with increasing d, full blue line in Fig. 14(a). It follows an approximately linear behavior with 13 meV/nm. Mode B, in contrast, remains constant in energy. The small apparent oscillations of the bright mode position may be due to the interference with the interband transitions, since they entirely overlap (see Fig. 13), making it hard to capture the real behavior of the mode. The FWHM is approximately constant for mode D with a small increase for $d > 50$ nm (full red line in Fig. 14(a)), while mode B becomes broader for larger spheres because radiative damping scales with sphere volume (dashed red line).

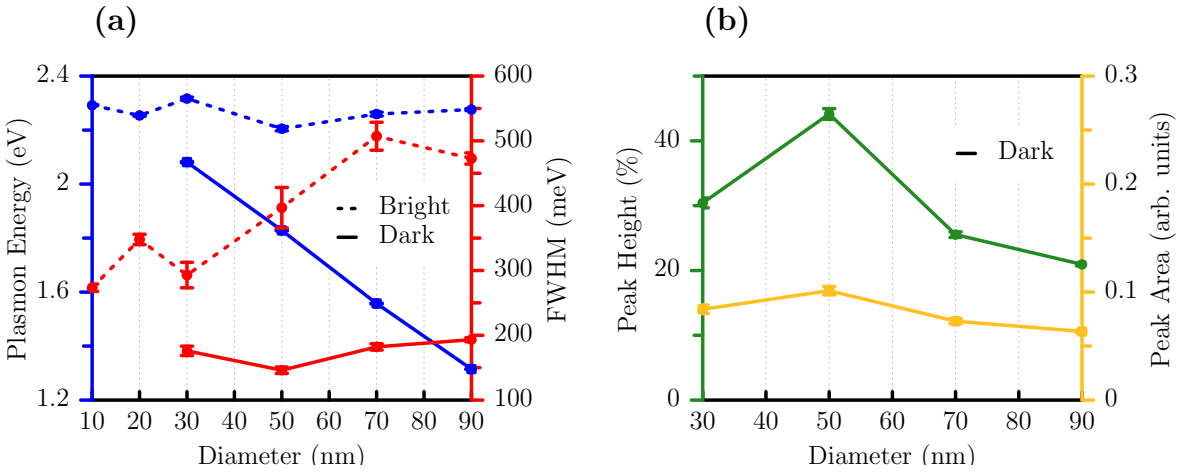

Figure 14: **(a)** Energy (E) and FWHM (γ) for the absorbance spectra in Fig. 12(a) as function of the diameter (d). The blue lines show the values of spectral position (E_j) while the red lines present the FWHM values (γ_j). The continuous lines correspond to the results for the dark mode (D) and the dashed lines to the bright mode (B). **(b)** Height (I) and area ($A = \pi I\gamma$) of the dark mode peaks in the absorbance spectra of Fig. 12(a) as function of the diameter (d). The green line shows the peak height of the dark mode ($I_D^{(Au)}$) while the yellow line presents the area of the peak ($A_D^{(Au)}$). In both panels, the error bar for each value is also provided, although some of them may not be visible as they are smaller than the point size.[42]

4.3.2 Influence of Lattice and Stacking

We now investigate the effect of the lattice and the stacking of the layers on the plasmonic properties of the bilayers. Figure 15 presents the optical response for bilayers with three different particle arrangements: layers formed by a hexagonal lattice with a hexagonal close-packed stacking (Hex-hcp) and with the particles aligned along z (Hex-align) and layers formed by a square lattice with aligned stacking (Sqr-align). The main features of the spectra are present in all three configurations. $E_D^{(Au)}$ is redshifted by 64 meV for Hex-align and blueshifted by 82 meV for Sqr-align with respect to Hex-hcp. This can be understood from the inset of Fig. 11(d). In the Hex-hcp stacking, the positive (negative) charges in the particle are closer to each other than in Hex-align, which causes a larger repulsion and blueshift. The blueshift for Sqr-align stacking stems from the lower particle density in this configuration compared to Hex-align. The smaller density results in less coupling and the plasmon energy has a smaller redshift than in the Hex-align configuration. The reduced coupling induced from the in-plane lattice configuration has a stronger effect than the layers stacking, as the blueshift in the Sqr-align configuration (compared to the Hex-align) is larger than the blueshift for Hex-hcp.

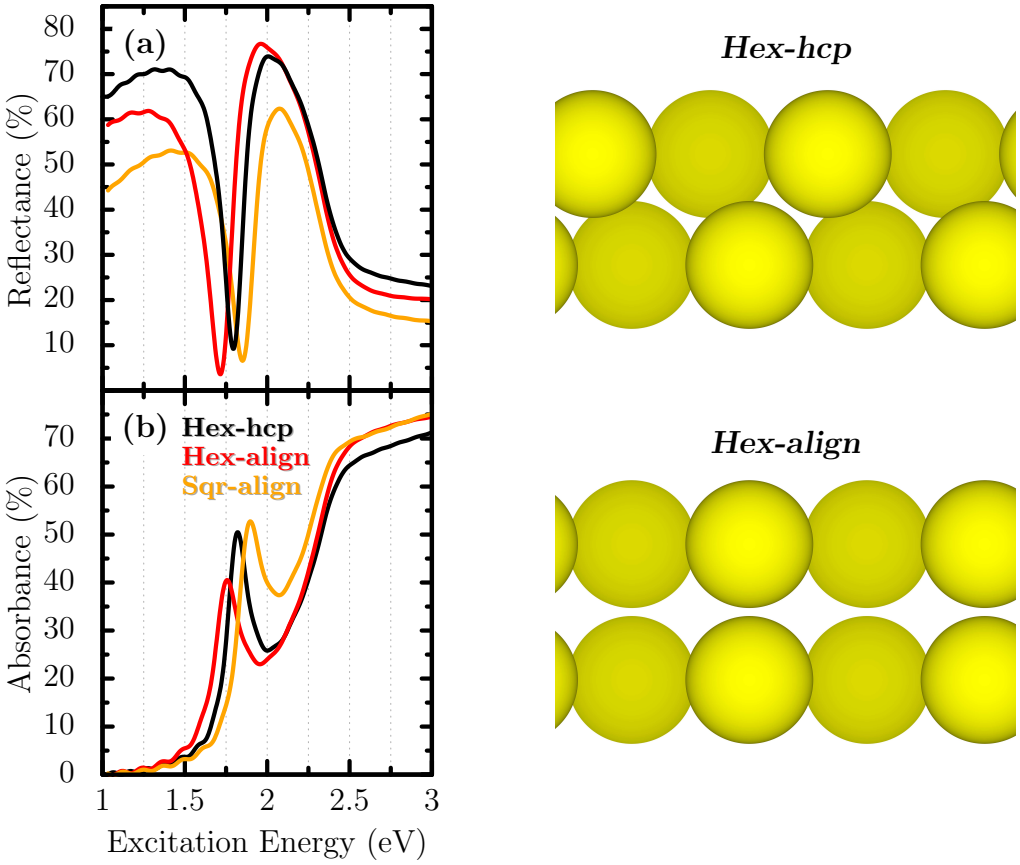

Figure 15: Influence of lattice and stacking on the **(a)** reflectance and **(b)** absorbance spectra. Three different configurations were studied: a hexagonal lattice with the layers in a hexagonal close-packed stacking (black lines and uppermost illustration) and aligned on top of each other (red lines and bottom illustration) and a square lattice with the particles aligned over each other (orange lines). In all cases, $d = 50$ nm and $g = 2$ nm were used as parameters.[42]

4.3.3 Gap Dependence

We now turn our attention to the influence of the gap size g ($g \equiv g_p = g_l$) on the optical properties. In Fig. 16 the absorbance and reflectance spectra for systems with varying g are shown. For gold, Figs. 16(a) and (b), the dark mode D starts to be effectively activated for $g \leq 10$ nm. As g is further reduced, $E_D^{(Au)}$ shifts towards smaller energies due to stronger coupling. The bright mode B shows a similar behavior with shrinking g as that observed for increasing d, i.e., it becomes completely suppressed by the interband transitions. Similar calculations for silver, Figs. 16(c) and (d), show qualitatively the same effect. Remarkably, even for $g = 20$ nm, the modes B and D of silver can still be distinguished, which does not occur for gold. By fitting the gold spectra similar to the diameter analysis, the strong redshift of $E_D^{(Au)}$ with decreasing g becomes apparent. Figure 17 shows that $E_D^{(Au)}$ (full blue line) goes from 2.2 to 1.6 eV when g changes from 10 to 1 nm. $\gamma_D^{(Au)}$ (full red line) is reduced when g decreases while $\gamma_B^{(Au)}$ (dashed red line) increases, see table 2. These results reveal that the energy of D can be tuned over a broad

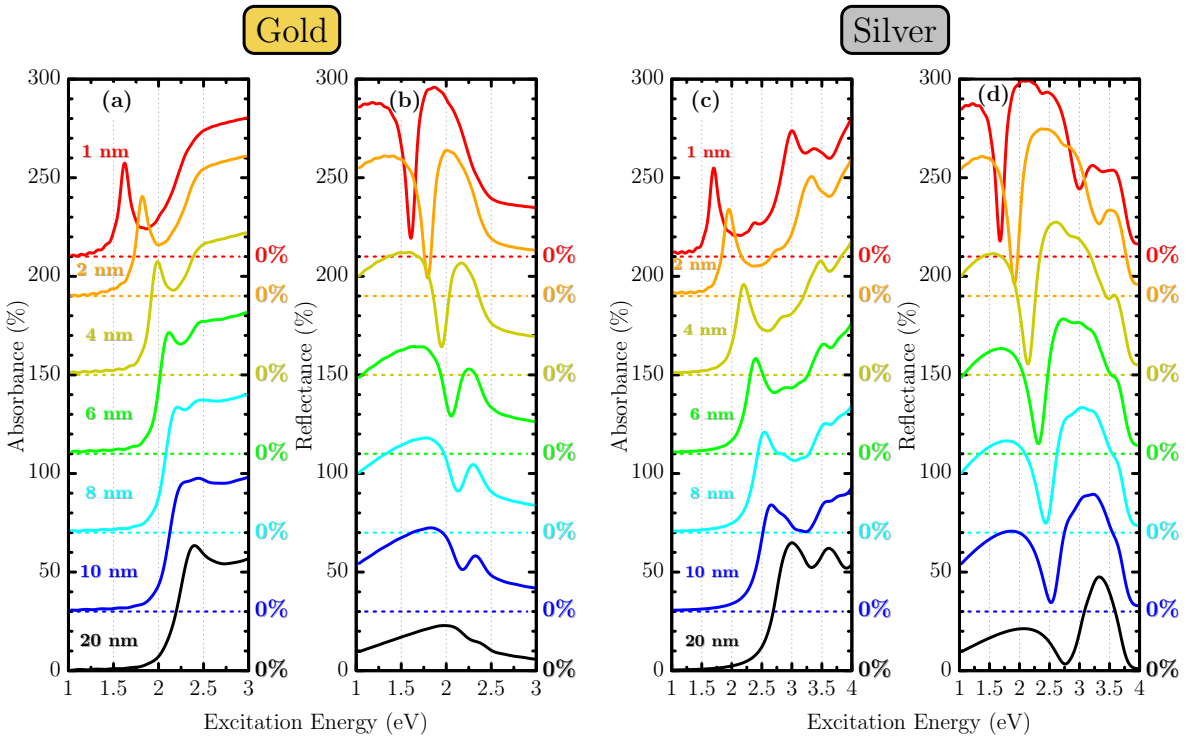

Figure 16: Absorbance and reflectance spectra for different gap sizes between all particles (g) with $d = 50$ nm. The color dashed lines indicate the offset of each spectrum. The left panels show the **(a)** absorbance and **(b)** reflectance spectra for gold while the right panels present the **(c)** absorbance and **(d)** reflectance spectra for silver. The dark modes of both gold and silver are effectively redshifted with decreasing g.[42]

spectral range in the visible/near-infrared by changing the gap size.[81] Colloidal samples in which g spreads over many values are expected to show D modes with broader FWHM than that of perfect NP crystals (simulated layers) as indeed observed experimentally[23].

We now investigate the influence of g_p and g_l separately. We consider hexagonal bilayers with aligned stacking (Hex-align), as g_p and g_l are linearly independent in this structure. Figure 18 shows that changes in the interparticle gap g_p affect the optical properties in a similar fashion as when varying both gaps simultaneously. A strong redshift of D is verified when g_p is reduced, which indicates that this mode is highly sensitive to it. Also, for $g_p > 10$ nm, this mode enters the interband transitions region and can no longer be identified.

Regarding the interlayer gap g_l dependence, Fig. 19 shows D already in the near-infrared ($E_D^{(Au)} = 1.28$ eV) for $g_l = 100$ nm and that it blueshifts with decreasing g_l. Note that the range in which g_l is varied ($2 - 100$ nm) is much larger than that used for g_p ($1 - 20$ nm), as, otherwise, no clear change would be observed. This fact suggests a low sensitivity of $E_D^{(Au)}$ on g_l, in contrast to the high sensitivity on g_p. This difference is explained by verifying that, for each NP and at any given distance, there are always more neighbors from the same layer (related to g_p) than from the other layer (related to

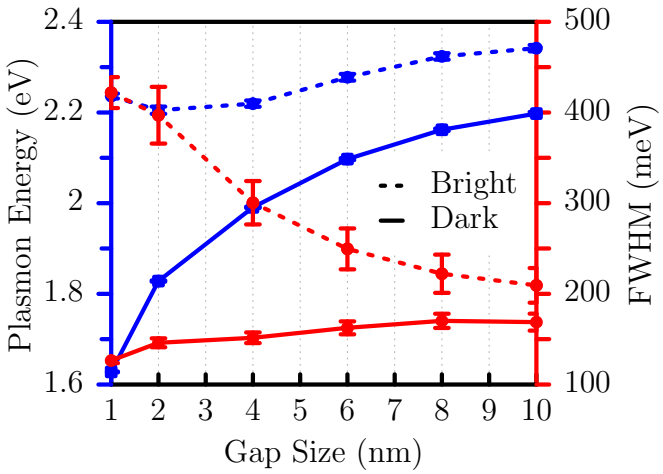

Figure 17: Fitted parameters for the absorbance spectra provided in Fig. 16(a) as function of the gap size (g). The blue lines show the values of spectral position (E_j) while the red lines present the FWHM values (γ_j). The continuous lines correspond to the results for mode D and the dashed lines to mode B. The error bar for each value is also provided and some of them may not be visible as they are smaller than the point size.[42]

g_l). For example, for the Hex-align configuration, each NP has six first neighbors within the same layer while there is just one from the other layer. Regardless of the magnitude of this effect, it appears surprising to observe a blueshift when g_l decreases considering the dipole hybridization model. One might expect the inverse in layer-layer coupling and a redshift with decreasing g_l.

In order to understand the observed behavior, we take a closer look at the interaction between two electric dipoles of the bilayer lattice, which is expressed by the following potential energy[82]

$$W_{ij} = \frac{e^{i\omega R_{ij}/c}}{4\pi\epsilon_0}\boldsymbol{p}_i \cdot \boldsymbol{p}_j \left[\left(\frac{1}{R_{ij}^3} - \frac{i\omega}{c}\frac{1}{R_{ij}^2}\right)\left(1 - 3\cos^2\phi_{ij}\right) - \frac{\omega^2}{c^2 R_{ij}}\sin^2\phi_{ij}\right] \tag{4.2}$$

where $\boldsymbol{p}_i$ is the dipole moment of the particle i, $R_{ij} \equiv |\boldsymbol{R}_{ij}|$ is the distance between particles i and j, ϕ_{ij} is the angle between $\boldsymbol{R}_{ij}$ and the polarization direction of the incident field, ω is the angular frequency of the incident field, c is the light speed in vacuum, and ϵ_0 is the vacuum permittivity. From Eq. (4.2), it is clear that W_{ij} can be either positive or negative depending on ϕ_{ij}. In Fig. 20(a), we illustrate that, for mode D and a given particle i in one layer, there are regions in which the dipole-dipole interaction is attractive (red regions) and others in which it is repulsive (blue regions). These regions are separated by the two dashed lines in the figure, which represent two cones in 3D space and indicate the exact angle ϕ_0 at which W_{ij} changes sign. Considering the effect of decreasing g_l, more particles get inside the repulsive regions and the overall interaction between the layers becomes more repulsive. This means that the mode moves towards higher energies, thus explaining the observed blueshift.

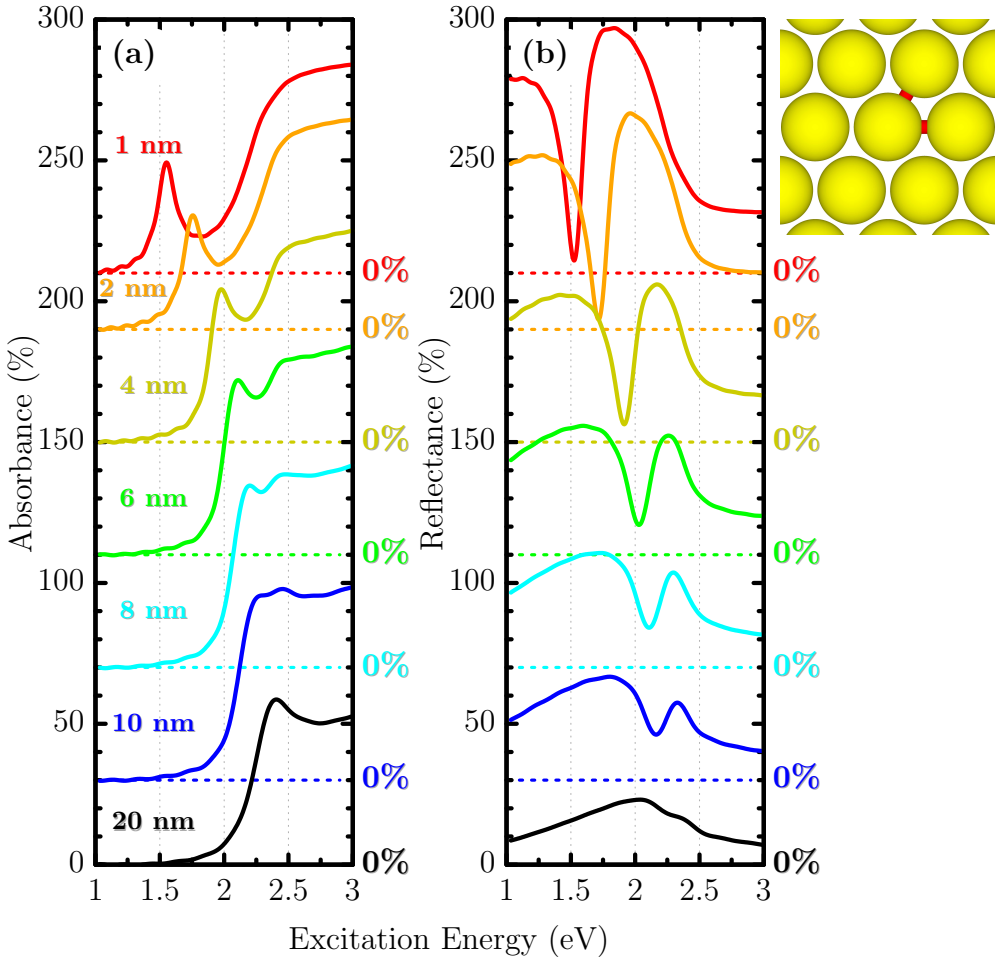

Figure 18: **(a)** Absorbance and **(b)** reflectance spectra for different interparticle gaps g_p. The gold bilayers have $d = 50$ nm and $g_l = 2$ nm. Aligned layer stacking was used. The color dashed lines indicate the offset of each spectrum and g_p is represented by the small red lines in rightmost illustration.[42]

It is worth noting that previous studies on similar systems observed a redshift when g_l diminishes, e.g., MIM vertical dimers[28,62], MIM pentamers[29] and MIM nanodisk arrays[26]. The apparent contradiction to our results is explained by the fact that the distance between adjacent MIM NPs (corresponding to g_p) is much larger in Refs. 26, 28, 29 and 62 than the g_p considered here. Consequently, the coupling between these MIM NPs is not strong enough for a similar blueshift to be verified. The blueshift occurs when g_p is sufficiently small for NPs to be able to move from the attractive region to the repulsive region when g_l is reduced. We can estimate the minimum g_p necessary for a redshift to occur when the layer distance is decreasing starting from a given height. It turns out that this minimum g_p needs to be very large for a possible redshift be observed. In Fig. 19 for example, g_p needs to be greater than 130 nm for a redshift to be observed starting from a g_l of 50 nm. At this regime, the particles are too far apart for the dark mode to be effectively excited (as observed in Fig. 18), meaning that the previously reported redshifts are not expected to appear in the layers of metallic nanospheres.

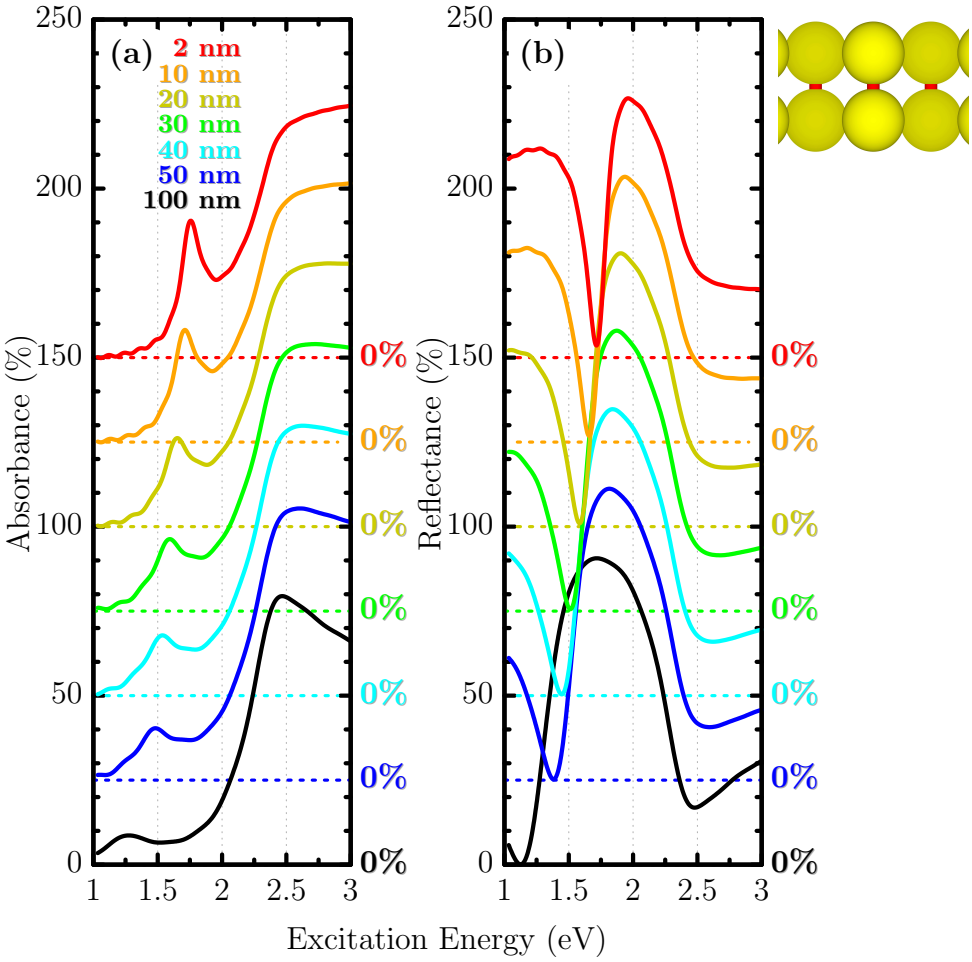

Figure 19: **(a)** Absorbance and **(b)** reflectance spectra for gold bilayers with different g_l ($d =$ 50 nm, $g_p = 2$ nm, aligned stacking). The color dashed lines indicate the offset of each spectrum and g_l is presented as the small red lines in the rightmost panel.[42]

Equation (4.2) may also be used to understand why no strong redshift occurs for mode B in the monolayer when g_p is reduced. In this case, there are also regions of attractive and repulsive interactions, see Fig. 20(b). However, the gap size does not significantly affect the number of particles in each region, which means that the redshift is not related to a change in this number. The slight redshift in Fig. 8 is caused by the bonding coupling between the particles in the red regions of Fig. 20(b), which is slightly stronger than the antibonding coupling between the particles in the blue regions. Similar explanations apply to the redshifts observed for the bright mode in silver bilayers when d increases and g decreases.

4.3.4 Nearfield

We finally turn our attention to the nearfield characteristics of the bilayers. Figure 21 displays the enhancement factor $EF = \frac{|\boldsymbol{E}|}{|\boldsymbol{E}_{inc}|}$ of the nearfield amplitude at the most

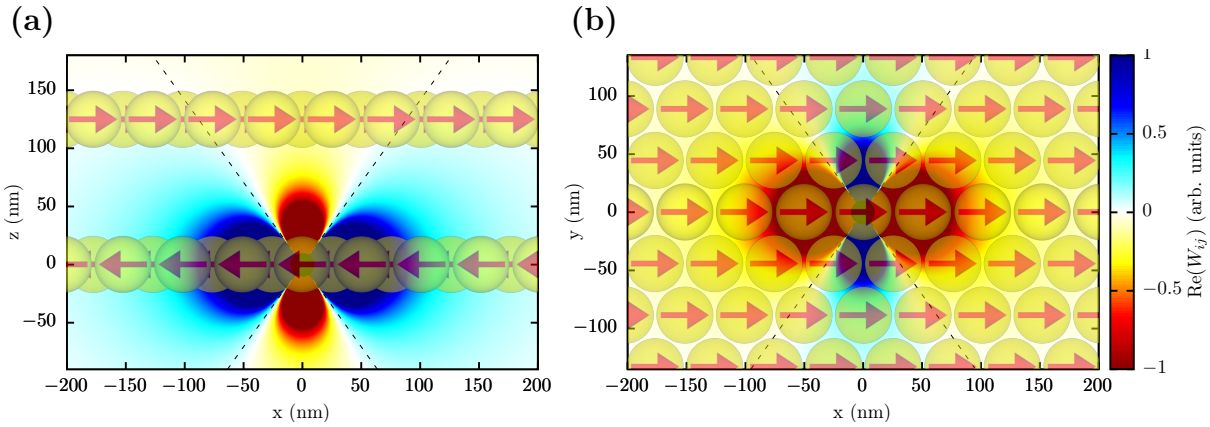

Figure 20: Mapping of the real part of the dipole-dipole interaction W_{ij} between a central dipole and **(a)** all dipoles in the other layer and **(b)** all other dipoles in the same layer. Panel **(a)** shows the side view of a bilayer in the dipole configuration of mode D and panel **(b)** the top view of a monolayer in mode B configuration. An illustration of the NPs is superimposed to the mappings for a better comprehension. The arrows represent the dipole moment in each particle and the dashed lines separate the regions where the dipole-dipole interaction has opposite signs.[42]

relevant regions of the gold bilayer with $d = 50$ nm and $g = 2$ nm, i.e., the system analyzed in Fig. 11. At $E_{exc} = E_D^{(Au)}$, strong enhancement factors of up to $EF = 55$ are observed in the regions around the particle gaps. Such an EF reinforces the potential of these layers for SERS applications, since an SERS enhancement of up to $\left(\frac{|\boldsymbol{E}|}{|\boldsymbol{E}_{inc}|}\right)^4 \approx 10^7$ is expected. Even though this SERS enhancement is lower than for a NP dimer, the layers have a larger density of hotspots that can provide enhancement. While a dimer has just one hotspot, the bilayers have approximately 10^3 hotspots per μm^2. Taking into account the tunability with particles size and gap, the potential of this mode and, consequently, of these materials, for applications in surface-enhanced spectroscopy becomes evident.

Remarkably, there are no significant hotspots between the layers. The hotspots are found at the g_p voids such that the most intense places are for those oriented parallel to the incident light. The absence of enhancement between the layers is explained by the orientation of all dipoles within the layers, as the dipoles have no component along the z direction. Our nearfield results are in good agreement with other mappings previously reported in the literature[25,30].

4.4 Experimental Verification

The simulation predictions were checked by measuring the far-field properties of self-assembly samples of gold nanospheres with $d = 46$ nm and $g = 2$ nm.[17] The transmission electron microscopy (TEM) image in Fig. 24(b) shows an example of colloidal mono- and bilayer. As polystyrene and oleylamine molecules are used as ligands for the

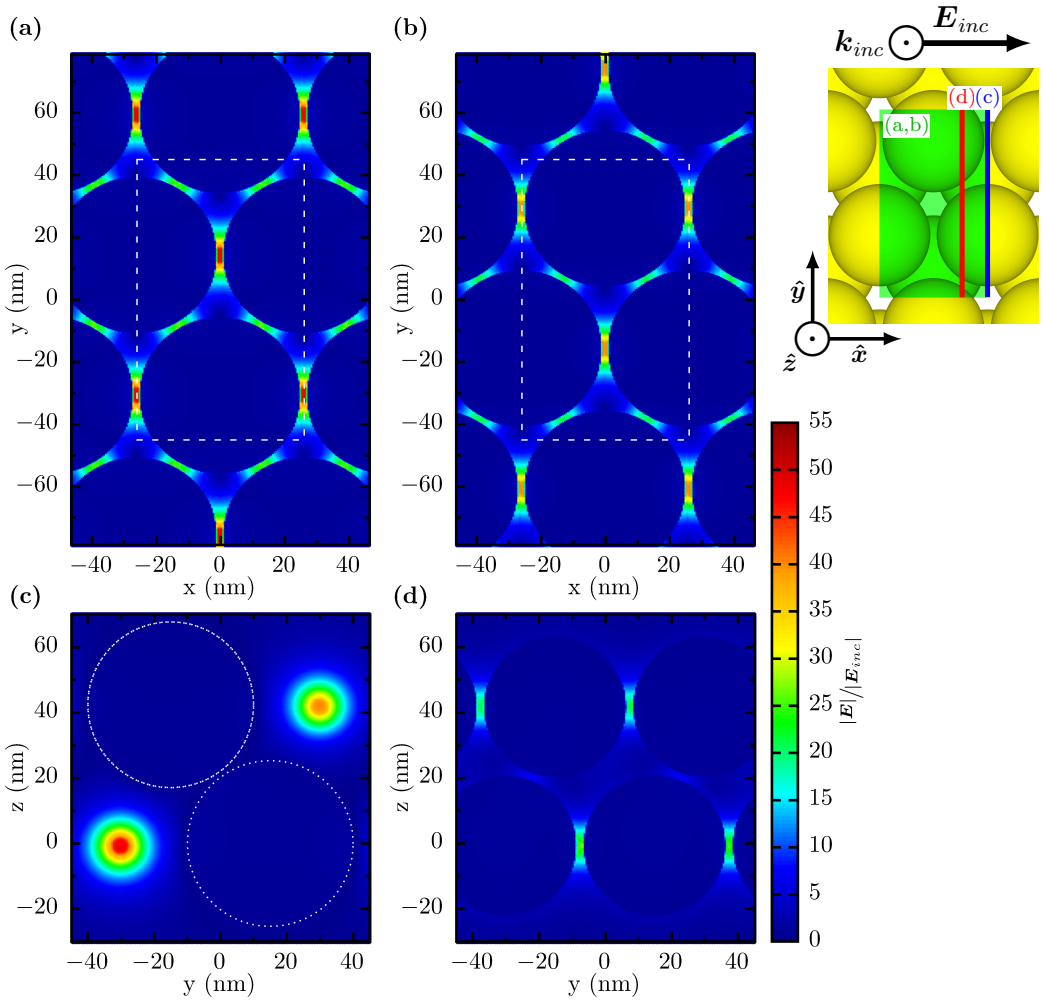

Figure 21: Nearfield enhancement factor mapping for the gold bilayer of Fig. 11 at the excitation energy of mode D ($E_{exc} = E_D^{(Au)} = 1.82$ eV). The two upper panels correspond to xy planes connecting the centers of each sphere in the **(a)** first layer and **(b)** second layer. The unit cells of each respective layer are indicated by the white dashed lines at the panels and by the green area shown in the inset. The two lower panels are related to the yz planes illustrated in the inset by **(c)** the blue line and **(d)** the red line.[42]

gold NPs during the synthesis process, the surrounding medium needs to be considered as an effective medium with constant refractive index $n = 1.4$. Fig. 22 shows then the simulated optical response of mono- and bilayers with the samples parameters. These new simulations are in total accordance to the systematic investigations of Secs. 4.2 and 4.3. The monolayer absorbance in Fig. 22(a) is characterized mainly by the IT contribution with a small peak at 2.25 eV related to the bright plasmon mode. The bilayer absorbance spectrum in Fig. 22(b) shows a peak at 1.44 eV that corresponds to the dark mode D. The bright plasmon peak is completely damped by the IT and, consequently, is no longer visible in the bilayer spectrum. The redshift of mode D in comparison to the spectra from Sec. 4.3 is caused by the higher refractive index of the surrounding medium used in the new simulations. During the synthesis process, the colloidal layers were deposited

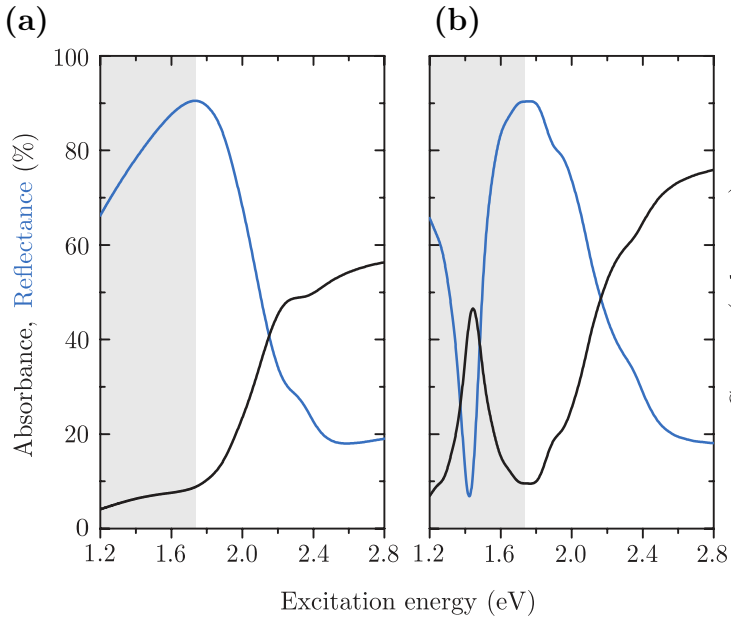

Figure 22: Simulated reflectance and absorbance spectra of the **(a)** monolayer and **(b)** bilayer correspondent to the colloidal self-assembly samples ($d = 46$ nm, $g = 2$ nm, hcp stacking and $n = 1.4$). The gray area indicates the region where the dark mode peak is expected to appear. Reprinted with permission from Ref 23.

onto a TEM grid with a 10 nm thick amorphous carbon film. Although this film was not considered into the systematic calculations, we verified that it does not affect the overall optical response of the system, as observed in Fig. 23.

Let's move now to the measurements. The transmittance and reflectance spectra of the gold NP layers were measured with a home-built microabsorbance spectrometer. These experiments were performed by Niclas S. Mueller from the group of Prof. Stephanie Reich in the Freie Universität Berlin in Berlin, Germany. Fig. 24(a) illustrates how the experiment works. The incident light is generated by a super-continuum laser (Fianium, SC-400-4) whose spectral range is from 450 nm to 2400 nm. After passing through a linear polarizer and a series of light filters and beam splitters, that tunes the laser power and spectral range, the laser is focused into the sample by an objective lens. The transmitted light is collected by a second objective lens, which is connected to a spectrometer by using an optical fiber. The spectrometer then generates the transmittance (T) spectra. The reflected light is collected by the same objetive lens used to focus the laser beam onto the sample. By using beam splitters, part of the outgoing reflected light ends up into the spectrometer and the reflectance (R) spectra is measured. The absorbance A is then determined as $1 - T - R$. Another part of reflected light goes into an optical microscope camera, enabling to find the same position in the sample for both transmittance and reflectance measurements as well as identify mono-, bi- and trilayer regions, see Fig. 24(c). The same spectrometer and optical fiber were used for both transmittance and reflectance measurements, which means the spectra had to be measured separately. For

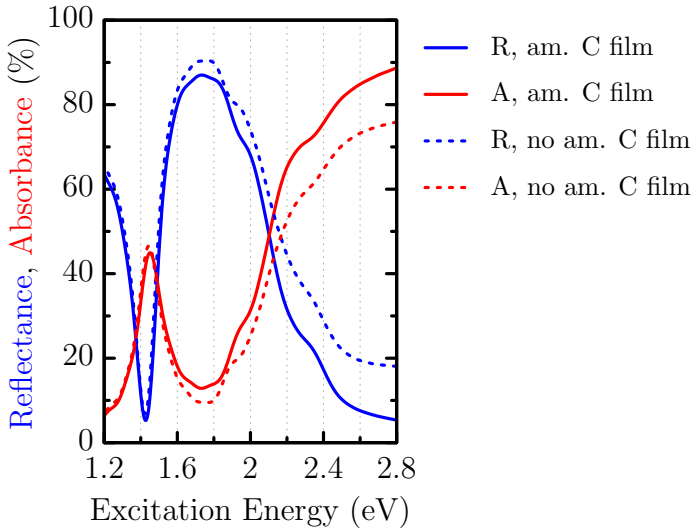

Figure 23: Influence of the amorphous carbon film on the optical response of a bilayer. The continuous lines show the simulated absorbance (red) and reflectance (blue) spectra for the gold bilayer on top of a 10 nm thick amorphous carbon film. Despite the amorphous carbon film, the system is the same from Fig. 22(b), whose spectra are also included here (dotted lines) for better visualization of the amorphous carbon film influence. The film affects mainly the spectral region with energies larger than 2.2 eV, increasing the absorbance and decreasing the reflectance by approximately 10%. The dark mode excitation remains unchanged. For the dielectric function of the amorphous carbon, the experimental data from Ref. 55 were used.

further details on the experimental setup, please refer to Ref. 23.

Fig. 25 shows the measured spectra for both mono- and bilayers at two different places. The corresponding simulated spectra are also included, see Figs. 22(c) and (f). The matching between the simulation predictions and the experimental measurements for both mono- and bilayers is evident. The monolayer measured spectra, Figs. 25(a) and (b), are dominated by the IT tail above 2 eV[2,74] and, consequently, the bright mode peak predicted at 2.25 eV is practically invisible. We verify that the dark mode is successfully excited at the colloidal bilayers, producing the absorbance peak at 1.53 eV and the reflectance dip at 1.48 eV, gray shaded area of Figs. 25(d) and (e). The same optical response is verified at different places throughout the sample, which assures that the experimental results are robust. The results for place 2, Figs. 25(b) and (e), show clearly this similarity.

By comparing Figs. 25(d) and (e) with Fig. 22(b), it becomes clear that the simulated linewidth ($\approx$ 180 meV) is much narrower than the linewidth for the measured samples ($\approx$ 360 meV). This broadening in the measured peaks stems from the fact that the colloidal layers are not perfect crystals, as the simulated with FDTD. From the TEM image in Fig. 24(b), we observe that there are fluctuations in both d and g. From the analysis in Secs. 4.3.1 and 4.3.3, we noticed that the resonance energy $E_D^{(Au)}$ is strongly influenced by such parameters (See Figs. 14 and 17). In order to verify this assumption, we performed

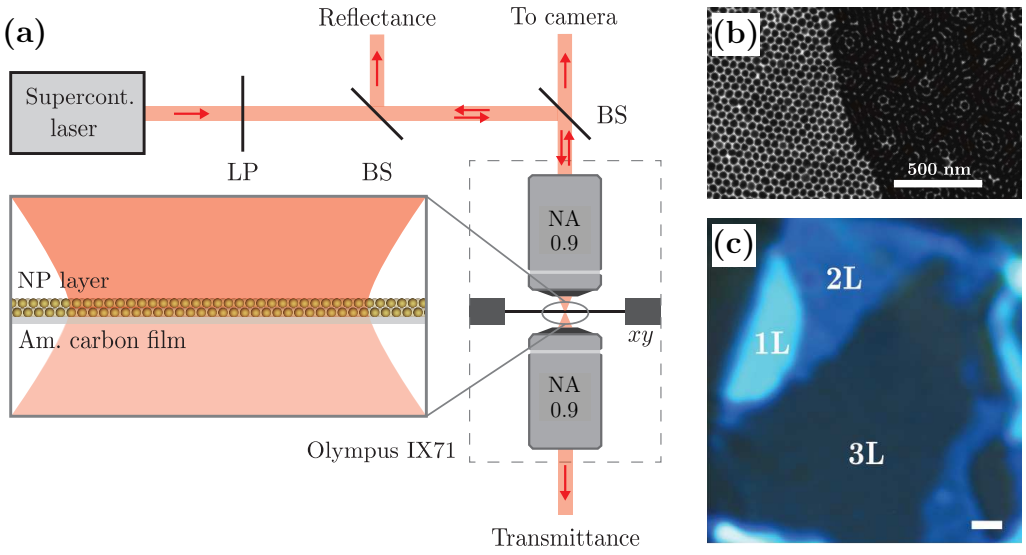

Figure 24: **(a)** Illustration scheme of experimental apparatus used to measure the optical response of the colloidal layers (Microabsorbance Measurements). A supercontinuum laser generates the laser beam (red line and arrows), which passes through a linear polarizer (LP) and some filters (not shown) and beam splitters (BS). The beam is then focused by an objective lens into the sample (zoomed area in the inset). The transmitted light is captured by a second objective and guided via optical fiber to a spectrometer to measure the transmittance. The reflected laser beam is separated by a beam splitter (BS) into a portion that goes into an optical microscope camera and another that is sent via optical fiber to a spectrometer to measure reflectance. **(b)** TEM image of a colloidal gold monolayer (left side) and bilayer (right side) sample. The monolayer is very close to a crystalline lattice with very few vacancies and small variations in particle size and distance. The bilayer shows a Moiré pattern, which suggests a non-zero twist angle between the layers. The samples were synthesized with the self-assembly technique developed by Schulz *et al.*[17]. Reprinted with permission from Ref. 23. **(c)** Optical microscopy image (camera) of a sample spot with mono- (1L), bi- (2L), and trilayer (3L) regions. The change in contrast helps to identify the different layer numbers. The scale bar (bottom right corner) is 1μm. Reprinted with permission from Ref. 24.

simulations for three gap sizes (1.5 nm, 2 nm and 2.5 nm) and average out the three spectra to see if the broadening appears. Fig. 26 shows the three calculated spectra for the bilayers and the average spectra are shown in Figs. 25(c) and (f) for mono- and bilayer, respectively. As expected, by averaging out the spectra, we were able to reproduce remarkably well the broadening of the dark mode peak for the colloidal samples. The influence of the numerical aperture of the focused laser beam was investigated and no considerable changes in the optical response of the layers were noted.[23] Thus, the larger linewidth of the experimental plasmon peaks is unambiguously caused by the spreading in the sample gap size.

The Moiré patterns in Fig. 24(b) indicates that there is a twist angle between the layers. As we verified in Sec. 4.3.2, the stacking between the layers does not substantially affect the plasmonic properties of the system and that is the reason for the nice matching between the hcp stacking results with the experiments without further analysis. For the

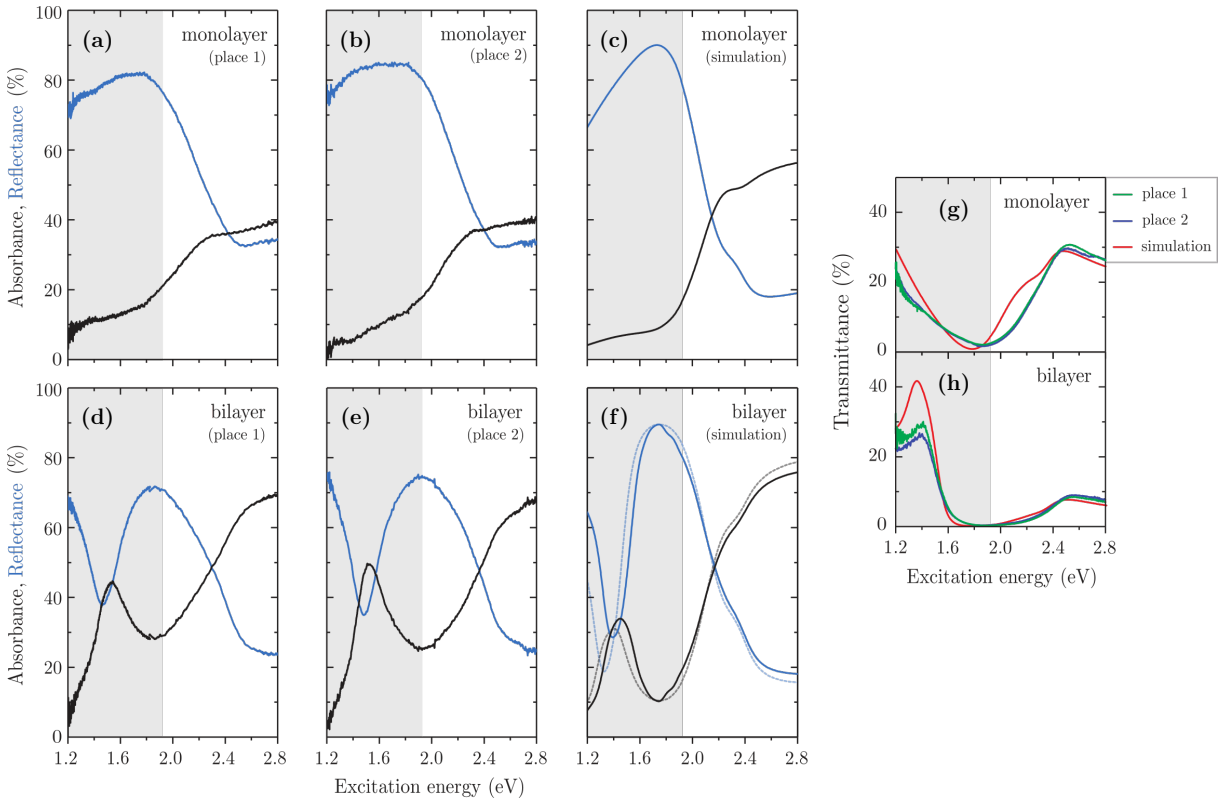

Figure 25: Reflectance (blue lines) and absorbance (black lines) spectra measured for colloidal **(a)** and **(b)** monolayers and **(d)** and **(e)** bilayers of gold NPs using microabsorbance spectroscopy. Measurements in two different places in the sample are provided. The dark plasmon mode is excited for both bilayers and the gray area indicates the region where its characteristic absorbance peak is expected to appear. The corresponding simulated spectra are shown for both **(c)** monolayer and **(f)** bilayer. These spectra were calculated as the average of the spectra for three gap sizes (g) of 1.5 nm, 2.0 nm and 2.5 nm with $d = 46$ nm,and $n = 1.4$ (Same parameters of Fig. 22), see Fig. 26. The corresponding transmittance spectra to each absorbance and reflectance spectra are also provided for both **(g)** monolayers and **(h)** bilayers. The solid lines show the spectra for the hcp stacking while the dotted lines present the spectra for the aligned stacking. Reprinted with permission from Ref 23.

sake of completeness, we included in Fig. 25(f) (dotted lines) the result of the average spectra for the bilayers in Hex-align configuration (layers perfectly aligned on top of each other), which confirms that the overall optical response remains unchanged.

4.5 Nanoparticle Trilayers to Multilayers

We will now explore the plasmonics for gold self-assemblies with larger layer number. Fig. 27(b) shows the simulated optical response of a trilayer. The spectra shows clearly the excitation of two modes, one at 1.55 eV and another at 1.2 eV. The plasmon peak at 1.55 eV has a linewidth of only 80 meV, being then 50% narrower than the dark plasmon peak excited in the bilayer (mode D). From the current profile shown in Fig.

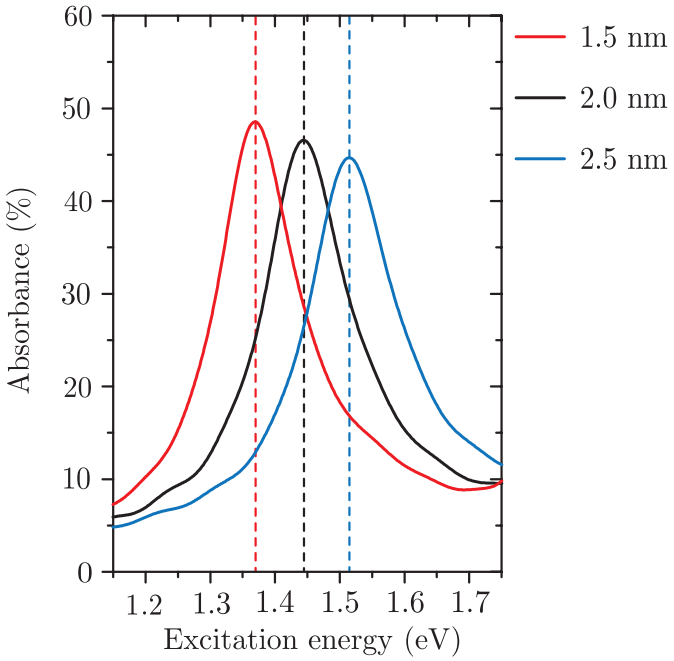

Figure 26: Simulated absorbance spectra that were used to produce the average spectra of Fig. 25(f) (solid line). All bilayers have $d = 46$ nm and $n = 1.4$. Three gap sizes were considered: $g = 1.5$ nm (red line), $g = 2.0$ nm (black line) and $g = 2.5$ nm (blue line). Reprinted with permission from Ref 23.

27(c), it is clear that the two modes are dark plasmon modes as they do not have a net dipole moment. These modes can be seen as symmetric (1.2 eV) and antisymmetric (1.55 eV) combinations of mode D (1.44 eV) in the bilayers of Fig. 22(b), as shown in the hybridization diagram of Fig. 27(e). The mode at 1.2 eV is the natural correspondent of the bilayer mode D since it also has an antiparallel dipole configuration between the outer layers. For the plasmon peak at 1.55 eV, the dipoles of each layer are oriented in the opposite direction with respect to its neighboring layers. Such mode can only be excited due to the high refractive index of the layers as metamaterials[76]. Inside the layers, the light wavelength is shrunk to almost one order of magnitude of its value in vacuum. At this extreme light shrinking regime, this dark mode can be easily excited by field retardation, similarly to the excitation of the bilayer mode D (Sec. 4.3). The microabsorbance measurements in Fig. 27(a) confirm the simulated spectra. Due to the inhomogeneous broadening discussed in Sec. 4.4, the measured linewidth of the 1.55 eV peak is 220 meV, which is still 40% smaller than the measured linewidth of bilayer mode D. The peak at 1.2 eV can be only partially observed as it is in the range limit of the experiment.

When further increasing the number of layers, a clear tendency is observed. Fig. 28(a) presents the simulated absorbance spectra of a bilayer up to a pentalayer. As expected, each new layer included generates a new dark plasmon mode. The new dark mode is always the mode where all neighboring layers has antiparallel dipole moments, as shown

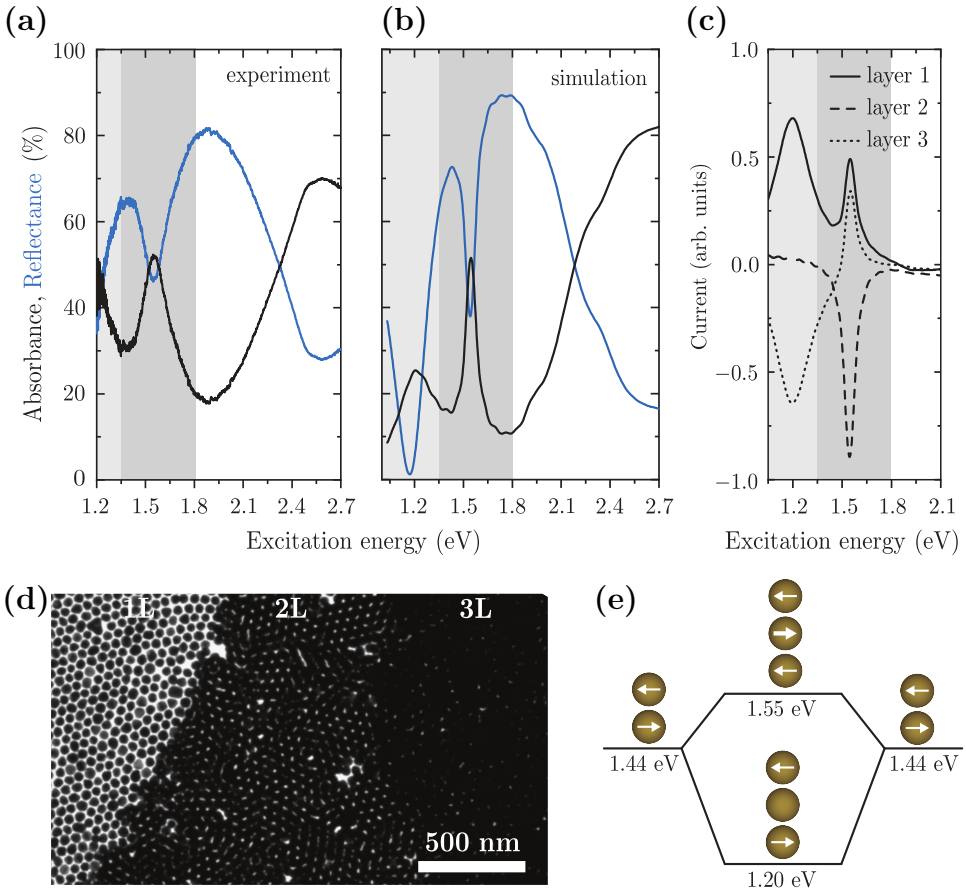

Figure 27: Plasmon excitations in a trilayer of gold NPs. **(a)** Experimental absorbance (black line) and reflectance (blue line) of a trilayer region in the colloidal samples. **(b)** Simulated spectra corresponding to the colloidal trilayer ($d = 46$ nm, $g = 2$ nm, hcp stacking and $n = 1.4$). **(c)** Current profile of each layer as function of the excitation energy, showing the dipole configuration of the excited plasmons. The plotted quantity is $< J_E >$, i.e., the spatial average of the electrical current density ($\boldsymbol{J}$) component parallel to the polarization direction ($\boldsymbol{E}_{inc}$). The incident light hits layer 1 first. The distinct shaded areas in the plots separate the excitation regions of each dark mode. **(d)** TEM image showing a sample spot with mono- (1L), bi- (2L) and trilayer (3L) regions. **(e)** Hybridization diagram that depicts the trilayer dark modes as symmetric and antisymmetric combinations of the bilayer dark mode D. Reprinted with permission from Ref. 23.

by the insets in Fig. 28(a) and Figs. 28(c) and (d). The other peaks correspond to the modes excited for smaller layer numbers. These peaks are redshifted and become broader as the number of layers increases. This analysis shows then that a general gold NP self-assembly with m layers is expected to have $(m-1)$ dark plasmon modes excited when illuminated by linearly polarized light at normal incidence.[23]

Although the new dark modes remain with a high narrow absorbance peak, the absorbance peak for other modes tend to decrease while its transmittance increases. For the pentalayer case, for instance, the lowest-energy mode absorbs just 10% of the light while 90% of it is transmitted (Reflectance is zero for this mode), see Fig. 28(b). As the pentalayer is a highly close-packed metamaterial with 200 nm thickness, it is

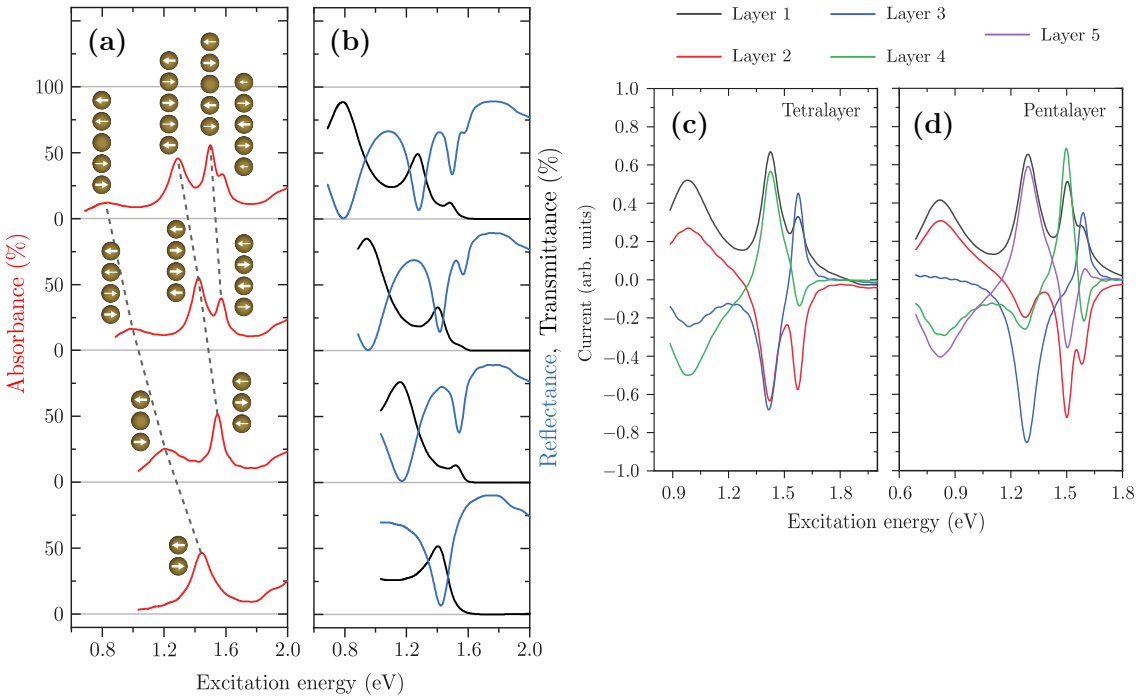

Figure 28: Influence of the layer number in the plasmonic properties of the layers. Simulated **(a)** absorbance, **(b)** reflectance and transmittance spectra for a bilayer (bottom curves) up to a pentalayer (top curves) of gold NPs ($d = 46$ nm, $g = 2$ nm, hcp stacking and $n = 1.4$). The dipole configuration of each plasmon peak is given by the insets in **(a)**. The dashed lines indicate how the modes evolve as the layer number increases. The current profile for the **(c)** tetra- and **(d)** pentalayer as a function of excitation energy is also provided. The plotted quantity is $< J_E >$ and the incident light hits layer 1 first. Reprinted with permission from Ref. 23.

quite surprising that most of the light passes through it without being either absorbed or reflected. To have a better idea, a gold film with only 140 nm thickness has a characteristic transmittance of just 10^{-4}% at $E_{exc} = 0.8$ eV[77]. The explanation for this high transmittance lies in the current distribution of the mode, see Fig. 28(d) and insets of Fig. 28(a). By analyzing the dipole configuration at the layers, it becomes evident that a standing wave pattern begins to appear as the layer number increases, allowing light to penetrate deep into the material and pass through it. A similar effect has been previously reported for crystals made of gold nanorods[83]. The underlying mechanism that explains thoroughly this behavior is related to plasmon-polaritons in deep strong coupling regime[84] and it is subject of ongoing studies.[85]

4.6 A Route to Hot-Electron Generation

Hot-electrons are highly energetic electrons that are in a non-thermal distribution, i.e., they are not in thermal equilibrium with the lattice. These hot carriers are known to be very useful for applications in photocatalysis and photovoltaic devices and surface

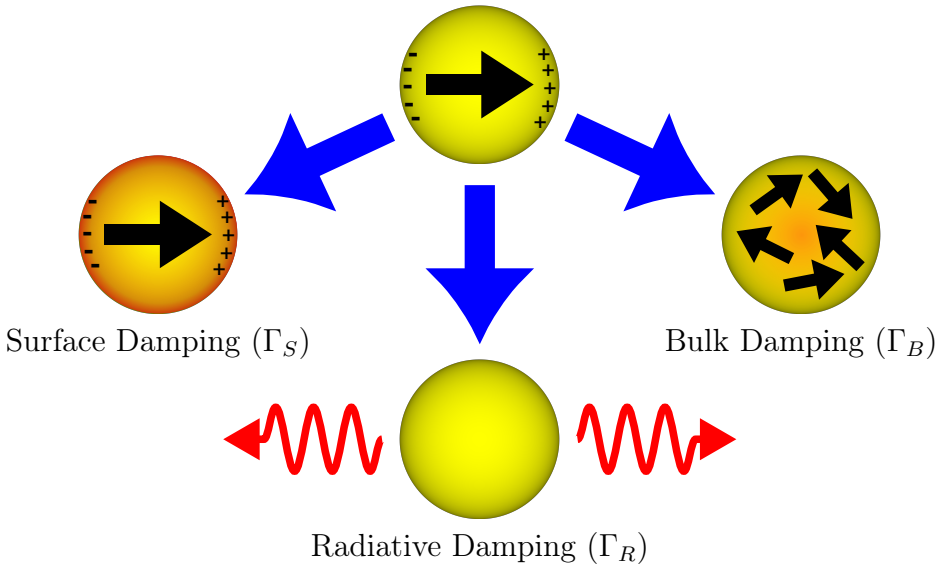

Figure 29: Illustration of the three main damping processes for plasmon decay: the intrinsic bulk damping Γ_B, the radiative damping Γ_R and the surface-mediated damping Γ_S. The surface damping Γ_S is the responsible for hot-electron generation.

imaging[86]. In the following section, we shall demonstrate that our NP layers are promising materials for hot-electrons harvesting[24].

As mentioned in Sec. 2.1, plasmons may decay in many different ways. In general, the plasmon decay can be defined as

$$\Gamma = \Gamma_B + \Gamma_R + \Gamma_S, \tag{4.3}$$

in which Γ_B is known as the intrinsic or Drude damping and accounts for all decay channels related to the bulk metal, Γ_S is the so-called surface or Landau damping, and Γ_R is the radiative damping and comprises the decay by the photon emission[2,87–90], as illustrated in Fig. 29. The hot-electron generation is related to the Landau damping Γ_S, as the surface breaks the crystalline quasi-momentum[87,91] and, consequently, leads to the excitation of highly energetic electrons. Therefore, in order to maximize the production of hot-electrons, the main idea is to optimize the metamaterial so that Γ_S becomes the predominant decay channel.

One strategy to follow is decreasing the NPs size to increase the surface-to-volume ratio. As demonstrated in Eq. 2.11, small NPs are known to be bad scatterers, so Γ_R is reduced in this case.[87,92–95] Indeed, the surface damping Γ_S becomes relevant for particle sizes below 10 nm.[2,89,92] On the other hand, the absorption CS also scales down with the NP size, as shown in Eq. 2.12, which means that less photons are exploited for hot-electron generation and the overall efficiency of the system is reduced.

Another route is to take advantage of the nearfield hotspots in NP Oligomers[91,96–98],

see Sec. 4.3.4. The hotspots create an anisotropy in the internal electric field of the NPs, which favours the Γ_S decay channel[87,97,99,100] and, consequently, the generation of hot-electrons. However, as the typical plasmon modes used for harvesting such hotspots are the bright modes, Γ_R becomes the preferred damping channel, i.e., most of the plasmon energy is used for the emission of photons and the plasmon decays rapidly in a few femtoseconds.[2,88,101]

As discussed in Secs. 4.1 and 4.3, dark plasmons typically interact weakly with far-field radiation as they have no net dipole moment[56]. This weak interaction makes difficult for the dark modes to decay by photon emission, which causes their Γ_R to be small in comparison to bright modes. This becomes evident by the difference in the linewidth between modes B and D for both gold and silver, see Fig. 13. Mode B is much broader than mode D due to its larger radiative damping Γ_R.[24] Thus, Γ_S should become the most relevant damping process in the decay of dark modes and we expect that the dark interlayer modes we studied in the previous sections should be excellent channels for hot-electron generation.

Fig. 30 shows results measured with time-resolved transient absorption (TTA) spectroscopy. This technique basically evaluate how the electronic density of states evolves after the system being optically excited. In brief, Fig. 30 shows the decay rate of plasmon excitations at $E_D^{(Au)}$, the energy of dark bilayer mode, when excited by a strong pump laser pulse at 1.27 eV.[‡] It is clear that, after the excitation by the pump pulse, most plasmons ($\approx 90\%$ of them) decay within the first 5 ps. However, the remaining $\approx 10\%$ of the plasmons sustain themselves in longer times (more than 50 ps) with very small decay rate. These are the plasmons that could be useful for hot-electron generation, as they are highly energetic and have very long lifetimes. This measurement is then the experimental evidence that hot-electrons can be generated at our colloidal layers.

In order to find an optimized system for plasmon-induced hot-electrons, it is important to consider how energetic are the plasmons and their lifetime, which is inversely proportional to the linewidth of the peak. We propose the quality factor $Q = \dfrac{E_D^{(Au)}}{\gamma_D^{(Au)}}$ as a good parameter for this analysis.[88,102] Considering d (the NPs diameter) as the optimization parameter, Fig. 31(a) shows the diameter dependence of the absorbance spectra for gold NP bilayers. Note that these spectra are similar to the discussed in Sec. 4.3.1 with the difference that the higher refractive index $n = 1.4$ used in the spectra of Fig. 31(a) causes all dark plasmon peaks to be redshifted in comparison to vacuum ($n = 1$). Although Fig. 31(a) seems to indicate that mode D gets narrower and more energetic for smaller NPs, the solid grey curve (circles) of Fig. 31(b) shows that the

[‡]For more information about the TTA measurements and how Fig. 30 is determined, please refer to Ref. 24. The details on these topics are out of this thesis scope.

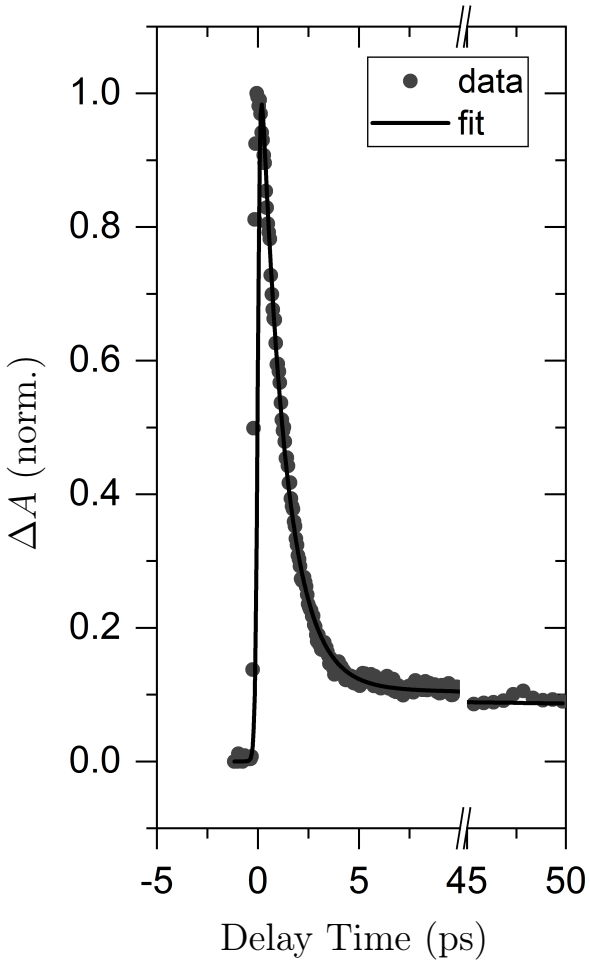

Figure 30: Normalized absorbance difference $\Delta A = A_{probe} - A_{pump}$ as function of the pump-probe delay time, i.e., the difference in the time that took for the pump pulse and the probe pulse to reach the sample. These results were measured with time-resolved transient absorption (TTA) spectroscopy on the gold colloidal samples with $d = 40$ nm and $g = 2$ nm. The excitation energy of the pump was set to 1.27 eV. The presented curve is then determined by measuring the TTA spectra for all pump-probe delay times and taking all resulting ΔA for the probe energy equal to $E_D^{(Au)}$. Reprinted with permission from Ref. 24.

resulting Q factor of mode D is expected to have a maximum value $Q_{max} = 22.5$ for $d = 25$ nm. This value Q_{max} is remarkably larger than the Q factor for isolated gold nanospheres of the same size, which is known to be $Q < 8$.[88] Note also that $\gamma_D^{(Au)}$ seems to become much larger for $d = 10$ nm, see Fig. 31(a). This apparent increase is actually caused by the overlap between modes D and B. As observed in Figs. 10 and 12, the IT gets weaker for smaller particles; therefore, mode B is not completely suppressed. Thus, the broad peak seen in Fig. 31(a) (black line) is the superposition of both modes.

Another feature that needs to be considered is the total number of plasmons that can be populated around the dark plasmon energy. As the hot-electron efficiency is expected to be proportional this population number, we can account for it by simply multiplying the Q factor by the peak area, see dashed grey curve in Fig. 31(b) (diamonds). It turns

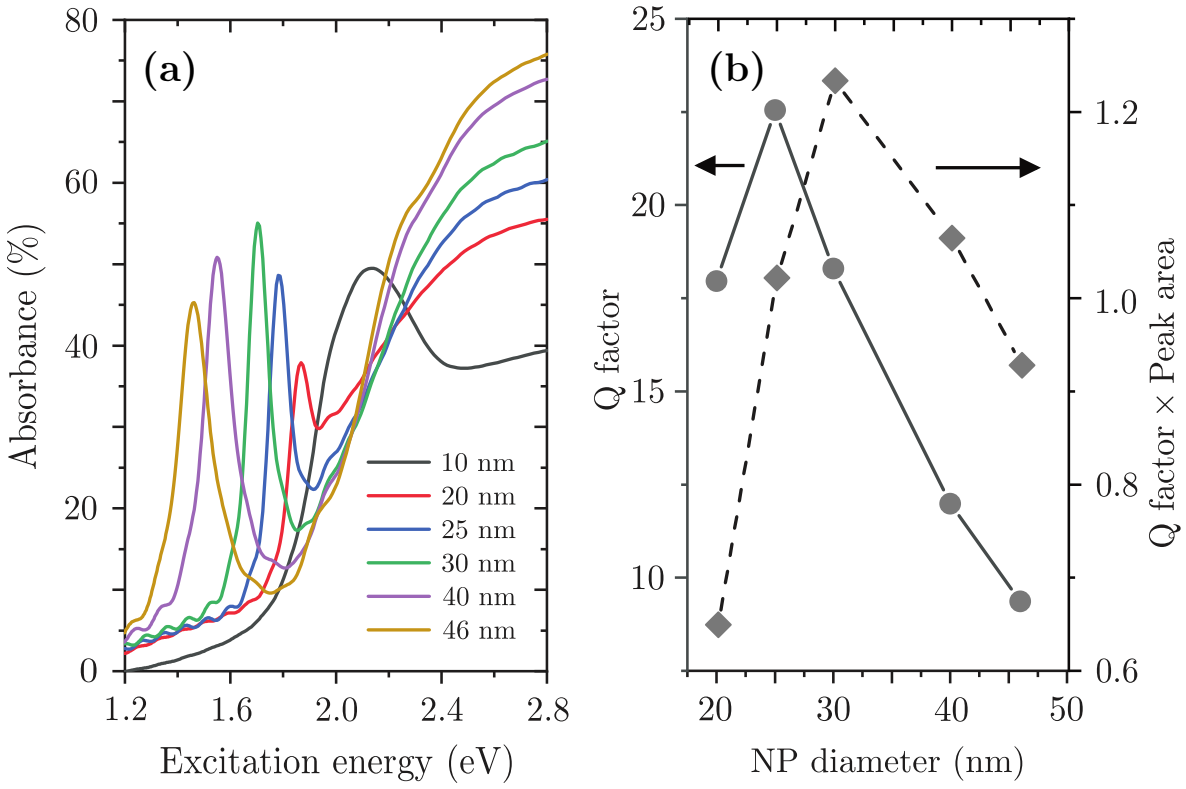

Figure 31: **(a)** Diameter dependence of the simulated absorbance in gold bilayers ($g = 2$ nm, hcp stacking and $n = 1.4$). **(b)** Q (Quality Factor) and Q times $A_D^{(Au)}$ (Peak Area) as a function of d (NPs diameter). Reprinted with permission from Ref. 24.

out that, among the bilayers, the optimal diameter for generating hot-electrons is expected to be 30 nm, a little larger than the value determined by the Q factor analysis. These predictions may be verified experimentally by performing TTA measurements on bilayer samples with different NP sizes.

4.7 Including a Gold Slab: Perfect Light Absorption

Finally, we studied the effect of placing the layers on a gold slab with a spacer separating them.[103–105] Fig. 32 shows the simulated absorbance (red line) and reflectance (blue line) of the bilayer from Fig. 22(b) on top of a gold substrate and a SiO_2 film of 100 nm thickness between them, as illustrated in Fig. 32(b). Mode D continues to be excited at the same energy but now it reaches the outstanding 100% light absorption. Note that the SiO_2 thickness makes the bilayer inversion center to be at $s \approx \frac{\lambda_{pl}}{4}$ above the gold slab, where λ_{pl} is the excitation wavelength of the plasmon mode D inside the SiO_2 medium. As the gold slab acts as a perfect mirror (no light is transmitted), the perfect light absorption stems partially from the fact that the reflected wave tends to cancel with the incoming wave, which reduces drastically the reflectance and, consequently, all light

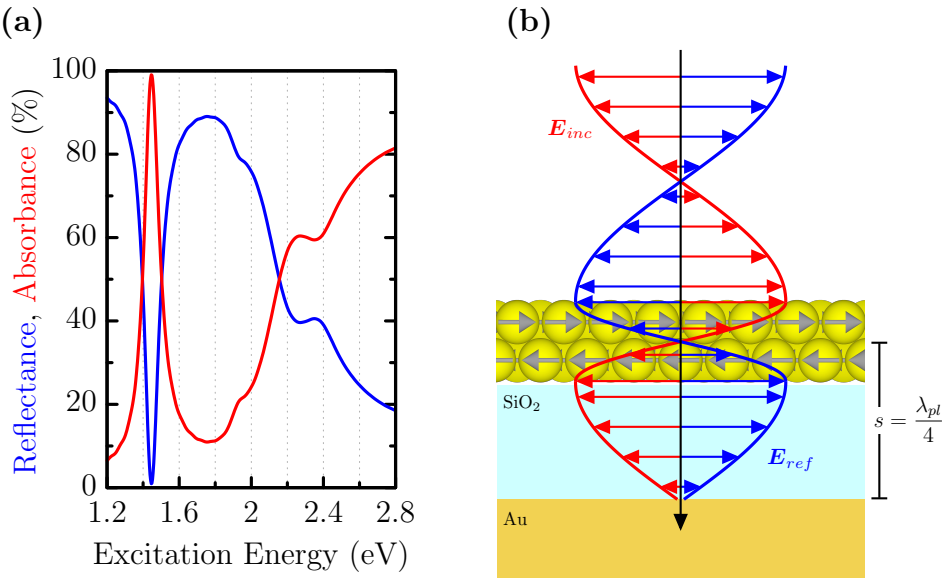

Figure 32: Influence of a reflective surface on the layers plasmonic properties. **(a)** Simulated absorbance (red) and reflectance (blue) of a gold bilayer deposited on a gold slab with a 100 nm thick SiO_2 film used as a spacer (d = 46 nm, g = 2 nm, hcp stacking and n = 1.4). The absorbance peak intensity of mode D of Fig. 22 remarkably increases to 100%. **(b)** The destructive interference between the incident ($\boldsymbol{E}_{inc}$) and reflected ($\boldsymbol{E}_{ref}$) electromagnetic field is partially the reason for this perfect absorption. The fields cancel out when the distance s between the gold slab and the bilayer center is equal to quarter the excitation wavelength of mode D.

tends to be absorbed by the system[§], as shown in Fig. 32(b).

The effect is totally related to the interplay between the distance s and the plasmon excitation wavelength λ_{pl}. Therefore, for colloidal bilayers with different d, we can adjust the SiO_2 thickness so that the new system (Bilayer+SiO_2+Slab) also exhibits this perfect absorption behavior. Although the perfect light absorption was previously observed in the literature for similar systems[106,107], a complete comprehension on how the optical response is affected by the distance between the bilayer and the gold mirror is still needed. Preliminary investigations have shown some interesting and unexpected results and an in-depth analysis of the simulations is necessary to understand the behavior. This analysis will be a topic for future studies.

[§]A deeper analysis is still necessary to fully explain this perfect absorption.

	d (nm)	g (nm)	α	I_B	E_B (eV)	γ_B (meV)	I_D	E_D (eV)	γ_D (meV)
Gold	10	2	0.471 ± 0.005	0.347 ± 0.005	2.292 ± 0.002	273 ± 6	—	—	—
Gold	20	2	0.754 ± 0.007	0.331 ± 0.005	2.254 ± 0.003	348 ± 8	—	—	—
Gold	30	2	0.893 ± 0.007	0.204 ± 0.005	2.317 ± 0.005	293 ± 20	0.304 ± 0.008	2.081 ± 0.002	176 ± 7
Gold	50	2	1.143 ± 0.010	0.175 ± 0.006	2.205 ± 0.008	397 ± 31	0.442 ± 0.008	1.828 ± 0.001	146 ± 5
Gold	70	2	1.212 ± 0.008	0.184 ± 0.004	2.259 ± 0.007	507 ± 22	0.255 ± 0.004	1.558 ± 0.002	182 ± 5
Gold	90	2	1.211 ± 0.005	0.244 ± 0.003	2.276 ± 0.003	473 ± 9	0.209 ± 0.002	1.315 ± 0.001	193 ± 3
Gold	50	1	1.103 ± 0.008	0.224 ± 0.005	2.236 ± 0.005	422 ± 17	0.433 ± 0.006	1.628 ± 0.001	126 ± 3
Gold	50	4	1.170 ± 0.008	0.213 ± 0.007	2.220 ± 0.007	300 ± 24	0.471 ± 0.010	1.991 ± 0.002	152 ± 6
Gold	50	6	1.153 ± 0.008	0.230 ± 0.010	2.278 ± 0.007	250 ± 23	0.453 ± 0.014	2.097 ± 0.002	163 ± 7
Gold	50	8	1.122 ± 0.008	0.229 ± 0.013	2.324 ± 0.007	222 ± 21	0.409 ± 0.016	2.162 ± 0.003	170 ± 8
Gold	50	10	1.087 ± 0.007	0.246 ± 0.015	2.342 ± 0.007	209 ± 19	0.344 ± 0.019	2.198 ± 0.004	169 ± 9
Silver	50	2	0.794 ± 0.010	0.557 ± 0.006	3.298 ± 0.006	830 ± 11	0.390 ± 0.004	1.972 ± 0.001	217 ± 4

Table 2: Values of the fitting parameters of Eq. (4.1) used in Figs. 13, 14 and 17. All values are for bilayers with hcp stacking.

5 Conclusions

In conclusion, we investigated the plasmonic properties of mono-, bi- and fewlayers made of gold and silver NPs when illuminated by linearly polarized light at normal incidence. We demonstrated by FDTD simulations the excitation of one bright plasmon mode in monolayers, characterized by a non-zero net dipole moment, and two plasmon modes in the bilayers: a bright mode and a dark mode that has a vanishing dipole moment. The dark mode was excited due to field retardation, inducing an anti-parallel dipole configuration in the bilayers. We observed that the field retardation becomes sufficiently large to excite the dark mode for particles whose diameter is above 30-50 nm, depending on the refractive index of the surrounding medium. and the dark mode is effectively activated. Also, the resonance energy and the linewidth of the dark mode can be tuned over a wide range of energies by varying the structural parameters of the system, such as particles size and their separation. For instance, its resonance energy is redshifted by more than 360 meV when changing the gap between the particles from 4 to 1 nm. Nearfield hotspots where the field amplitude is enhanced by 55 times were observed. This enhancement is ideal for SERS as the NP layers provide not only SERS enhancement factors on order of 10^7 but also have 10^3 hotspots per μm^2. We verified that gold and silver have qualitatively similar optical responses. Besides the differences in the plasmon energy and linewidth of their dark modes, the bright mode of silver bilayers could be visualized in the spectra as it is not completely damped by the interband transitions. For gold, this bright mode is totally suppressed and is not visible in most of the presented spectra.

The dark mode excitation was successfully demonstrated by micro-absorbance spectroscopy in bi- and trilayers of self-assembled gold NPs. A prominent absorbance peak of almost 50% was measured in the near-infrared for bilayers with NPs of 46 nm size. This peak was unambiguously assigned to the dark plasmon mode by comparing with simulations. In the trilayers, a second dark mode with a FWHM 40% narrower than for the bilayer dark mode is excited. As the number of layers is further increased, the number of excited dark modes increases accordingly and we observed that a multilayer with m layers will produce $(m-1)$ dark plasmon peaks when illuminated by a plane linear light source. However, the dark modes tend to become standing waves for larger layer numbers, causing their absorbance to strongly decrease and light to be almost completely transmitted through the film.

We showed that the dark interlayer plasmons can be excellent channels for generating hot-electrons that can be used for photocatalytical applications. By using time-resolved pump-probe spectroscopy, we measured the decay rate of the plasmons after being excited.

It was demonstrated that a portion of these plasmons are sustained for more than 50 ps, indicating their potential as hot-electron generators. We predicted the optimal NP size for hot-electron generation by tuning it to favor the surface damping channel. Also, we verified that the inclusion of a gold slab as a subtrate for the layers enables the system to absorbe 100% of incident light in the dark mode resonance energy, an effect that can further maximize the emission of hot-electrons. Beyond SERS and hot-electrons, the narrow peak width of the dark mode is also ideal for refractive index sensing. It is worth remembering that the self-assembly synthesis technique is low-cost, versatile and very precise, which allows the tunability of plasmonic properties as well as the scalability for large-scale applications.

As perspective, we are currently working on the plasmon-polariton effects in the layers. As mentioned in Sec. 4.5, we are studying the fundamental way that the layers coupled with light and so far we have verified that their coupling is particularly strong, known as deep strong light-matter coupling.[85] Only very few materials have this special coupling regime with light and this effect is opening the way for many new investigations on how this interaction works as well as for new applications of the noble-metal NP layers. Regarding the perfect optical absorption (Sec. 4.7), we still need to fully understand why a 100% absorbance was reached and analyze deeply the dependence of the optical response with the distance between the gold mirror and the bilayers. Afterwards, the investigation can be extended to study the behavior for larger number of layers (trilayers and so on) on top of the slab. Going further, we can explore other metals and investigate how their NP layers would respond optically. Aluminum is one example that it is known to have interesting plasmonic effects[108–110] (besides being a low cost and widely abundant element).

In summary, there are still a plenty of room for exciting investigations on these layered structure, being them either experimental or theoretical. Finally, all the discussions presented in this thesis, together with the already well developed methods for the materials synthesis, show how promising the noble-metal NP layers are for plasmonic applications, being also very intriguing from the theoretical point of view.

References

[1] E. C. L. Ru and P. G. Etchegoin. *Principles of surface enhanced Raman spectroscopy*. Elsevier, 1st edition, 2009. ISBN 9780874216561. doi: 10.1007/s13398-014-0173-7.2.

[2] S. A. Maier. *Plasmonics: Fundamentals and Applications*. Springer, New York, 2007. ISBN 0387331506. doi: 10.1007/0-387-37825-1.

[3] K. L. Kelly, E. Coronado, L. L. Zhao, and G. C. Schatz. The optical properties of metal nanoparticles: the influence of size, shape, and dielectric environment. *J. Phys. Chem. B*, 107:668–677, 2003. doi: 10.1021/jp026731y.

[4] D. K. Gramotnev and S. I. Bozhevolnyi. Plasmonics beyond the diffraction limit. *Nature Photonics*, 4(2):83–91, feb 2010. ISSN 1749-4885. doi: 10.1038/nphoton.2009.282.

[5] V. Flauraud, R. Regmi, P. M. Winkler, D. T. L. Alexander, H. Rigneault, N. F. Van Hulst, M. F. García-Parajo, J. Wenger, and J. Brugger. In-plane plasmonic antenna arrays with surface nanogaps for giant fluorescence enhancement. *Nano Letters*, 17:1703–1710, 2017. doi: 10.1021/acs.nanolett.6b04978.

[6] A. Hartstein, J. R. Kirtley, and J. C. Tsang. Enhancement of the infrared absorption from molecular monolayers with thin metal overlayers. *Phys. Rev. Lett.*, 45(3):201–204, 1980.

[7] F. Benz, M. K. Schmidt, A. Dreismann, R. Chikkaraddy, Y. Zhang, A. Demetriadou, C. Carnegie, H. Ohadi, B. de Nijs, R. Esteban, J. Aizpurua, and J. J. Baumberg. Single-molecule optomechanics in "picocavities". *Science*, 354(6313), 2016. doi: 10.1126/science.aag1322.

[8] R. Zhang, Y. Zhang, Z. C. Dong, S. Jiang, C. Zhang, L. G. Chen, L. Zhang, Y. Liao, J. Aizpurua, Y. Luo, J. L. Yang, and J. G. Hou. Chemical mapping of a single molecule by plasmon-enhanced Raman scattering. *Nature*, 498:82–86, 2013. doi: 10.1038/nature12151.

[9] K. Kneipp, Y. Wang, H. Kneipp, L. T. Perelman, I. Itzkan, R. R. Dasari, and M. S. Feld. Single molecule detection using surface-enhanced Raman scattering (SERS). *Phys. Rev. Lett.*, 78(9):1667–1670, 1997.

[10] M. Moskovits. Surface-enhanced spectroscopy. *Reviews of Modern Physics*, 57(3): 783–826, 1985.

[11] J. A. Schuller, E. S. Barnard, W. Cai, Y. C. Jun, J. S. White, and M. L.

Brongersma. Plasmonics for extreme light concentration and manipulation. *Nature Materials*, 9:193–204, 2010. doi: 10.1038/nmat2630.

[12] K. M. Mayer and J. H. Hafner. Localized surface plasmon resonance sensors. *Chemical Reviews*, 111(6):3828–3857, 2011. ISSN 00092665. doi: 10.1021/cr100313v.

[13] H. A. Atwater and A. Polman. Plasmonics for improved photovoltaic devices. *Nature Materials*, 9:205–213, 2010. doi: 10.1038/nmat2629.

[14] M. B. Ross, C. A. Mirkin, and G. C. Schatz. Optical properties of one-, two-, and three-dimensional arrays of plasmonic nanostructures. *The Journal of Physical Chemistry C*, 120(2):816–830, jan 2016. ISSN 1932-7447. doi: 10.1021/acs.jpcc.5b10800.

[15] Z. Nie, A. Petukhova, and E. Kumacheva. Properties and emerging applications of self-assembled structures made from inorganic nanoparticles. *Nature Nanotechnology*, 5, 2009. doi: 10.1038/nnano.2009.453.

[16] S. Julin, S. Nummelin, M. A. Kostiainen, and V. Linko. DNA nanostructure-directed assembly of metal nanoparticle superlattices. *Journal of Nanoparticle Research*, 20:119, 2018. ISSN 1572896X. doi: 10.1007/s11051-018-4225-3.

[17] F. Schulz, S. Tober, and H. Lange. Size-dependent phase transfer functionalization of gold nanoparticles to promote well-ordered self-assembly. *Langmuir*, 33: 14437–14444, 2017. doi: 10.1021/acs.langmuir.7b03600.

[18] J. Gong, R. S. Newman, M. Engel, M. Zhao, F. Bian, S. C. Glotzer, and Z. Tang. Shape-dependent ordering of gold nanocrystals into large-scale superlattices. *Nature Communications*, 8, 2017. doi: 10.1038/ncomms14038.

[19] C. Hanske, G. González-Rubio, C. Hamon, P. Formentín, E. Modin, A. Chuvilin, A. Guerrero-Martínez, L. F. Marsal, and L. M. Liz-Marzán. Large-scale plasmonic pyramidal supercrystals via templated self-assembly of monodisperse gold nanospheres. *The Journal of Physical Chemistry C*, 121(20):10899–10906, may 2017. ISSN 1932-7447. doi: 10.1021/acs.jpcc.6b12161.

[20] A. Klinkova, R. M. Choueiri, and E. Kumacheva. Self-assembled plasmonic nanostructures. *Chem. Soc. Rev*, 43:3976–3991, 2014. doi: 10.1039/c3cs60341e.

[21] M. Grzelczak, J. Vermant, E. M. Furst, and L. M. Liz-Marzán. Directed self-assembly of nanoparticles. *ACS Nano*, 4(7):3591–3605, 2010. doi: 10.1021/nn100869j.

[22] A. R. Tao, D. P. Ceperley, P. Sinsermsuksakul, A. R. Neureuther, and P. Yang.

Self-organized silver nanoparticles for three-dimensional plasmonic crystals. *Nano Letters*, 8(11):4033–4038, 2008. doi: 10.1021/nl802877h.

[23] N. S. Mueller, B. G. M. Vieira, F. Schulz, P. Kusch, V. Oddone, E. B. Barros, H. Lange, and S. Reich. Dark interlayer plasmons in colloidal gold nanoparticle bi- and few-layers. *ACS Photonics*, 5(10):3962–3969, oct 2018. ISSN 2330-4022. doi: 10.1021/acsphotonics.8b00898.

[24] N. S. Mueller, B. G. M. Vieira, D. Höing, F. Schulz, E. B. Barros, H. Lange, and S. Reich. Direct optical excitation of dark plasmons for hot electron generation. *Faraday Discuss.*, 214:159–173, 2019. doi: 10.1039/C8FD00149A.

[25] H. Alaeian and J. A. Dionne. Plasmon nanoparticle superlattices as optical-frequency magnetic metamaterials. *Optics Express*, 20(14):15781–15796, 2012. ISSN 1094-4087. doi: 10.1364/OE.20.015781.

[26] Y. C. Chang, S. M. Wang, H. C. Chung, C. B. Tseng, and S. H. Chang. Observation of absorption-dominated bonding dark plasmon mode from metal-insulator-metal nanodisk arrays fabricated by nanospherical-lens lithography. *ACS Nano*, 6(4): 3390–3396, 2012. ISSN 19360851. doi: 10.1021/nn300420x.

[27] H. Wang, X. Wang, C. Yan, H. Zhao, J. Zhang, C. Santschi, and O. J. Martin. Full color generation using silver tandem nanodisks. *ACS Nano*, 11(5):4419–4427, 2017. ISSN 1936086X. doi: 10.1021/acsnano.6b08465.

[28] M. Frederiksen, V. E. Bochenkov, R. Ogaki, and D. S. Sutherland. Onset of bonding plasmon hybridization preceded by gap modes in dielectric splitting of metal disks. *Nano Letters*, 13(12):6033–6039, 2013. ISSN 15306984. doi: 10.1021/nl4032567.

[29] R. Verre, Z. J. Yang, T. Shegai, and M. Käll. Optical magnetism and plasmonic Fano resonances in metal-insulator-metal oligomers. *Nano Letters*, 15 (3):1952–1958, 2015. ISSN 15306992. doi: 10.1021/nl504802r.

[30] Z.-j. Cai, G.-q. Liu, Z.-q. Liu, X.-s. Liu, P.-p. Pan, S. Huang, Y. Wang, M.-l. Liu, and H. Gao. Subradiant, superradiant plasmon modes and Fano resonance in a multilayer nanocylinder array standing on a thin metal film. *Plasmonics*, 11(2): 683–688, apr 2016. ISSN 1557-1955. doi: 10.1007/s11468-015-0103-3.

[31] W. Zhou and T. W. Odom. Tunable subradiant lattice plasmons by out-of-plane dipolar interactions. *Nature Nanotechnology*, 6(7):423–427, jul 2011. ISSN 1748-3387. doi: 10.1038/nnano.2011.72.

[32] S. Panaro, A. Nazir, C. Liberale, G. Das, H. Wang, F. De Angelis, R. Proietti Zaccaria, E. Di Fabrizio, and A. Toma. Dark to bright mode conversion on dipolar nanoantennas: a symmetry-breaking approach. *ACS Photonics*, 1(4):310–314, apr 2014. ISSN 2330-4022. doi: 10.1021/ph500044w.

[33] A. D. Humphrey, N. Meinzer, T. A. Starkey, and W. L. Barnes. Surface lattice resonances in plasmonic arrays of asymmetric disc dimers. *ACS Photonics*, 3: 634–639, 2016. doi: 10.1021/acsphotonics.5b00727.

[34] L. Chuntonov and G. Haran. Trimeric plasmonic molecules: the role of symmetry. *Nano Letters*, 11(6):2440–2445, jun 2011. ISSN 1530-6984. doi: 10.1021/nl2008532.

[35] M. Liu, T.-W. Lee, S. K. Gray, P. Guyot-Sionnest, and M. Pelton. Excitation of dark plasmons in metal nanoparticles by a localized emitter. *Phys. Rev. Lett.*, 102: 107401, 2009. doi: 10.1103/PhysRevLett.102.107401.

[36] F. Peyskens, A. Z. Subramanian, P. Neutens, A. Dhakal, P. Van Dorpe, N. Le Thomas, and R. Baets. Bright and dark plasmon resonances of nanoplasmonic antennas evanescently coupled with a silicon nitride waveguide. *Optics Express*, 23 (3):3088, feb 2015. ISSN 1094-4087. doi: 10.1364/OE.23.003088.

[37] T. Pakizeh, M. S. Abrishamian, N. Granpayeh, A. Dmitriev, and M. Käll. Magnetic-field enhancement in gold nanosandwiches. *Optics express*, 14(18): 8240–8246, 2006. ISSN 1094-4087. doi: 10.1364/OE.14.008240.

[38] J. Sancho-Parramon and S. Bosch. Dark modes and Fano resonances in plasmonic clusters excited by cylindrical vector beams. *ACS Nano*, 6(9):8415–8423, 2012. ISSN 8415-8423. doi: 10.1021/nn303243p.

[39] D. E. Gómez, Z. Q. Teo, M. Altissimo, T. J. Davis, S. Earl, and A. Roberts. The dark side of plasmonics. *Nano Letters*, 13:3722–3728, 2013. doi: 10.1021/nl401656e.

[40] K. Sakai, K. Nomura, T. Yamamoto, and K. Sasaki. Excitation of multipole plasmons by optical vortex beams. *Scientific Reports*, 5(1):8431, jul 2015. ISSN 2045-2322. doi: 10.1038/srep08431.

[41] B. Luk'yanchuk, N. I. Zheludev, S. A. Maier, N. J. Halas, P. Nordlander, H. Giessen, and C. T. Chong. The Fano resonance in plasmonic nanostructures and metamaterials. *Nature Materials*, 9(9):707–715, sep 2010. ISSN 1476-1122. doi: 10.1038/nmat2810.

[42] B. G. M. Vieira, N. S. Mueller, E. B. Barros, and S. Reich. Plasmonic Properties of Close-Packed Metallic Nanoparticle Mono- and Bilayers. *The Journal of Physical Chemistry C*, 123(29):17951–17960, jul 2019. ISSN 1932-7447. doi: 10.1021/acs.jpcc.9b03859.

[43] L. Novotny and B. Hecht. *Principles of Nano-Optics*. cambridge university press, Cambridge, 2nd edition, 2012. ISBN 9781107005464.

[44] P. B. Johnson and R. W. Christy. Optical constants of the noble metals. *Phys. Rev. B*, 6:4370–4379, Dec 1972. doi: 10.1103/PhysRevB.6.4370.

[45] A. Trügler. URL http://physik.uni-graz.at/~atr/research.html.

[46] D. Boyer, P. Tamarat, A. Maali, B. Lounis, and M. Orrit. Photothermal imaging of nanometer-sized metal particles among scatterers. *Science*, 297(5584):1160–1163, 2002. ISSN 0036-8075. doi: 10.1126/science.1073765.

[47] S. A. Maier. *Plasmonics: Fundamentals and Applications*, chapter 5, page 65. In Maier[2], 2007. ISBN 0387331506. doi: 10.1007/0-387-37825-1.

[48] L. Novotny and B. Hecht. *Principles of Nano-Optics*, chapter 12, page 398. In Novotny and Hecht[43], 2nd edition, 2012. ISBN 9781107005464.

[49] P. Nordlander, C. Oubre, E. Prodan, K. Li, and M. I. Stockman. Plasmon hybridization in nanoparticle dimers. *Nano Lett.*, 4(5):899–903, 2004. doi: 10.1021/nl049681c.

[50] E. Prodan. A Hybridization Model for the Plasmon Response of Complex Nanostructures. *Science*, 302(5644):419–422, oct 2003. ISSN 0036-8075. doi: 10.1126/science.1089171.

[51] E. Prodan and P. Nordlander. Plasmon hybridization in spherical nanoparticles. *Journal of Chemical Physics*, 120(11):5444–5454, 2004. ISSN 00219606. doi: 10.1063/1.1647518.

[52] K. Yee. Numerical solution of initial boundary value problems involving maxwell's equations in isotropic media. *IEEE Transactions on Antennas and Propagation*, 14(3):302–307, May 1966. ISSN 0018-926X. doi: 10.1109/TAP.1966.1138693.

[53] J. B. Schneider. *Understanding the Finite-Difference Time-Domain Method*. 2012.

[54] E. D. Palik. *Handbook of Optical Constants of Solids*, volume 1 of *Academic Press Handbook*. Academic Press, 1st edition, 1985. ISBN 978-0125444200.

[55] J. I. Larruquert, L. V. Rodríguez-de Marcos, J. A. Méndez, P. J. Martin, and A. Bendavid. High reflectance ta-C coatings in the extreme ultraviolet. *Optics Express*, 21(23):27537, nov 2013. ISSN 1094-4087. doi: 10.1364/OE.21.027537.

[56] M.-W. Chu, V. Myroshnychenko, C. H. Chen, J.-P. Deng, C.-Y. Mou, and F. J. García de Abajo. Probing bright and dark surface-plasmon modes in individual and coupled noble metal nanoparticles using an electron beam. *Nano Letters*, 9(1): 399–404, jan 2009. ISSN 1530-6984. doi: 10.1021/nl803270x.

[57] A. Yanai, M. Grajower, G. M. Lerman, M. Hentschel, H. Giessen, and U. Levy. Near-and far-field properties of plasmonic oligomers under radially and azimuthally polarized light excitation. *ACS Nano*, 8(5):4969–4974, 2014. ISSN 4969-4974. doi: 10.1021/nn501031t.

[58] M. Hamermesh. *Group Theory and Its Application to Physical Problems*.

Addison-Wesley Publishing Company, U.S.A, 1964.

[59] M. S. Dresselhaus, G. Dresselhaus, and A. Jorio. *Group Theory: Application to the Physics of Condensed Matter*. Springer, Heidelberg, 2008.

[60] A. Jorio, N. S. Mueller, and S. Reich. Symmetry-derived selection rules for plasmon-enhanced Raman scattering. *Physical Review B*, 95(15):155409, apr 2017. ISSN 2469-9950. doi: 10.1103/PhysRevB.95.155409.

[61] U. Hohenester and A. Trügler. Mnpbem: A matlab toolbox for the simulation of plasmonic nanoparticles. *Comput. Phys. Commun.*, 183(2):370 – 381, 2012. ISSN 0010-4655. doi: https://doi.org/10.1016/j.cpc.2011.09.009.

[62] R. Ogier, L. Shao, M. Svedendahl, and M. Käll. Continuous-gradient plasmonic nanostructures fabricated by evaporation on a partially exposed rotating substrate. *Advanced Materials*, 28(23):4658–4664, jun 2016. ISSN 09359648. doi: 10.1002/adma.201600112.

[63] X. M. Zhang, J. J. Xiao, Q. Zhang, L. M. Li, and Y. Yao. Plasmonic TM-like cavity modes and the hybridization in multilayer metal-dielectric nanoantenna. *Optics Express*, 23(12):16122, 2015. ISSN 1094-4087. doi: 10.1364/OE.23.016122.

[64] A. Dmitriev, T. Pakizeh, M. Käll, and D. S. Sutherland. Gold-silica-gold nanosandwiches: Tunable bimodal plasmonic resonators. *Small*, 3(2):294–299, 2007. doi: 10.1002/smll.200600409.

[65] L. M. Liz-Marzán. Tailoring surface plasmons through the morphology and assembly of metal nanoparticles. *Langmuir*, 22:32–41, 2006. doi: 10.1021/la0513353.

[66] N. J. Halas, S. Lal, W.-S. Chang, S. Link, and P. Nordlander. Plasmons in strongly coupled metallic nanostructures. *Chemical Reviews*, 111(6):3913–3961, jun 2011. ISSN 0009-2665. doi: 10.1021/cr200061k.

[67] J. B. Lassiter, J. Aizpurua, L. I. Hernandez, D. W. Brandl, I. Romero, S. Lal, J. H. Hafner, P. Nordlander, and N. J. Halas. Close encounters between two nanoshells. *Nano Letters*, 8(4):1212–1218, apr 2008. ISSN 1530-6984. doi: 10.1021/nl080271o.

[68] E. C. L. Ru and P. G. Etchegoin. *Principles of surface enhanced Raman spectroscopy*, chapter 6, page 355. In Ru and Etchegoin[1], 1st edition, 2009. ISBN 9780874216561. doi: 10.1007/s13398-014-0173-7.2.

[69] S. K. Ghosh and T. Pal. Interparticle coupling effect on the surface plasmon resonance of gold nanoparticles: from theory to applications. *Chemical Reviews*, 107(11):4797–4862, nov 2007. ISSN 0009-2665. doi: 10.1021/cr0680282.

[70] I. Romero, J. Aizpurua, G. W. Bryant, and F. J. García De Abajo. Plasmons

in nearly touching metallic nanoparticles: singular response in the limit of touching dimers. *Optics Express*, 14(21):9988, 2006. ISSN 1094-4087. doi: 10.1364/OE.14.009988.

[71] Z. Zhong, S. Patskovskyy, P. Bouvrette, J. H. T. Luong, and A. Gedanken. The surface chemistry of Au colloids and their interactions with functional amino acids. *The Journal of Physical Chemistry B*, 108(13):4046–4052, apr 2004. ISSN 1520-6106. doi: 10.1021/jp037056a.

[72] K.-H. Su, Q.-H. Wei, X. Zhang, J. J. Mock, D. R. Smith, and S. Schultz. Interparticle coupling effects on plasmon resonances of nanogold particles. *Nano Letters*, 3(8):1087–1090, aug 2003. ISSN 1530-6984. doi: 10.1021/nl034197f.

[73] T. Jensen, L. Kelly, A. Lazarides, and G. C. Schatz. Electrodynamics of noble metal nanoparticles and nanoparticle clusters. *Journal of Cluster Science*, 10(2): 295–317, 1999.

[74] A. Pinchuk, G. Von Plessen, and U. Kreibig. Influence of interband electronic transitions on the optical absorption in metallic nanoparticles. *Journal of Physics D: Applied Physics*, 37:3133–3139, 2004. doi: 10.1088/0022-3727/37/22/012.

[75] S. Zhang and H. Xu. Tunable dark plasmons in a metallic nanocube dimer: toward ultimate sensitivity nanoplasmonic sensors. *Nanoscale*, 8:13722–13729, 2016. doi: 10.1039/c6nr03806a.

[76] R. Kim, K. Chung, J. Y. Kim, Y. Nam, S.-H. K. Park, and J. Shin. Metal nanoparticle array as a tunable refractive index material over broad visible and infrared wavelengths. *ACS Photonics*, 5(4):1188–1195, apr 2018. ISSN 2330-4022. doi: 10.1021/acsphotonics.7b01497.

[77] J. F. Lodenquai. Electromagnetic wave propagation in media with complex refractive indices and transmission through absorbing films. *American Journal of Physics*, 59:248, 1991. doi: 10.1119/1.16571.

[78] S. A. Kovalenko. Optical properties of thin metal films. *Semiconductor Physics, Quantum Electronics & Optoelectronics*, 2(3):13–20, 1999.

[79] E. C. L. Ru and P. G. Etchegoin. *Principles of surface enhanced Raman spectroscopy*, chapter Appendix E, page 532. In Ru and Etchegoin[1], 1st edition, 2009. ISBN 9780874216561. doi: 10.1007/s13398-014-0173-7.2.

[80] A. D. Rakic, A. B. Djurisic, J. M. Elazar, and M. L. Majewski. Optical properties of metallic films for vertical-cavity optoelectronic devices. *Applied optics*, 37(22): 5271–83, aug 1998. ISSN 1559-128X. doi: 10.1364/AO.37.005271.

[81] S. Ullrich, S. P. Scheeler, C. Pacholski, J. P. Spatz, and S. Kudera. Formation of

large 2d arrays of shape-controlled colloidal nanoparticles at variable interparticle distances. *Part. Part. Syst. Charact.*, 30(1):102–108, 2012. doi: 10.1002/ppsc.201200065.

[82] W. Greiner. *Classical Electrodynamics*, chapter 21, page 432. Springer, 1998. ISBN 0-387-94799-X.

[83] D. M. Solís, J. M. Taboada, F. Obelleiro, L. M. Liz-Marzán, and F. J. García de Abajo. Toward ultimate nanoplasmonics modeling. *ACS Nano*, 8(8):7559–7570, 2014. doi: 10.1021/nn5037703.

[84] A. F. Kockum, A. Miranowicz, S. De Liberato, S. Savasta, and F. Nori. Ultrastrong coupling between light and matter. *Nature Reviews Physics*, 1(January), 2018. ISSN 2522-5820. doi: 10.1038/s42254-018-0006-2.

[85] N. S. Mueller, Y. Okamura, B. G. M. Viera, S. Juergensen, H. Lange, E. B. Barros, F. Schulz, and S. Reich. Deep strong light-matter coupling in plasmonic nanoparticle crystals. Submitted.

[86] K. Marchuk and K. A. Willets. Localized surface plasmons and hot electrons. *Chemical Physics*, 445:95–104, dec 2014. ISSN 03010104. doi: 10.1016/j.chemphys.2014.10.016.

[87] G. V. Hartland, L. V. Besteiro, P. Johns, and A. O. Govorov. What's so hot about electrons in metal nanoparticles? *ACS Energy Letters*, 2(7):1641–1653, 2017. doi: 10.1021/acsenergylett.7b00333.

[88] C. Sönnichsen, T. Franzl, T. Wilk, G. von Plessen, J. Feldmann, O. Wilson, and P. Mulvaney. Drastic reduction of plasmon damping in gold nanorods. *Phys. Rev. Lett.*, 88:077402, Jan 2002. doi: 10.1103/PhysRevLett.88.077402.

[89] A. Crut, P. Maioli, N. Del Fatti, and F. Vallée. Optical absorption and scattering spectroscopies of single nano-objects. *Chemical Society reviews*, 43(11):3921—3956, June 2014. ISSN 0306-0012. doi: 10.1039/c3cs60367a.

[90] M. Liu, M. Pelton, and P. Guyot-Sionnest. Reduced damping of surface plasmons at low temperatures. *Phys. Rev. B*, 79:035418, Jan 2009. doi: 10.1103/PhysRevB.79.035418.

[91] L. V. Besteiro and A. O. Govorov. Amplified generation of hot electrons and quantum surface effects in nanoparticle dimers with plasmonic hot spots. *The Journal of Physical Chemistry C*, 120(34):19329–19339, 2016. doi: 10.1021/acs.jpcc.6b05968.

[92] J. A. Scholl, A. L. Koh, and J. A. Dionne. Quantum plasmon resonances of individual metallic nanoparticles. *Nature*, 483(7390):421–427, 2012. doi:

10.1038/nature10904.

[93] S. Link and M. A. El-Sayed. Spectral properties and relaxation dynamics of surface plasmon electronic oscillations in gold and silver nanodots and nanorods. *The Journal of Physical Chemistry B*, 103(40):8410–8426, 1999. doi: 10.1021/jp9917648.

[94] C. Novo, D. Gomez, J. Perez-Juste, Z. Zhang, H. Petrova, M. Reismann, P. Mulvaney, and G. V. Hartland. Contributions from radiation damping and surface scattering to the linewidth of the longitudinal plasmon band of gold nanorods: a single particle study. *Phys. Chem. Chem. Phys.*, 8:3540–3546, 2006. doi: 10.1039/B604856K.

[95] S. Berciaud, L. Cognet, P. Tamarat, and B. Lounis. Observation of intrinsic size effects in the optical response of individual gold nanoparticles. *Nano Letters*, 5(3):515–518, 2005. doi: 10.1021/nl050062t. PMID: 15755105.

[96] P. Christopher, H. Xin, A. Marimuthu, and S. Linic. Singular characteristics and unique chemical bond activation mechanisms of photocatalytic reactions on plasmonic nanostructures. *Nature Materials*, 11, 2012.

[97] A. Sousa-Castillo, M. Comesaña-Hermo, B. Rodríguez-González, M. Pérez-Lorenzo, Z. Wang, X.-T. Kong, A. O. Govorov, and M. A. Correa-Duarte. Boosting hot electron-driven photocatalysis through anisotropic plasmonic nanoparticles with hot spots in au–tio2 nanoarchitectures. *The Journal of Physical Chemistry C*, 120(21):11690–11699, 2016. doi: 10.1021/acs.jpcc.6b02370.

[98] H. Harutyunyan, A. B. F. Martinson, D. Rosenmann, L. K. Khorashad, L. V. Besteiro, A. O. Govorov, and G. P. Wiederrecht. Anomalous ultrafast dynamics of hot plasmonic electrons in nanostructures with hot spots. *Nature nanotechnology*, 10(9):770—774, September 2015. ISSN 1748-3387. doi: 10.1038/nnano.2015.165.

[99] H. Zhang and A. O. Govorov. Optical generation of hot plasmonic carriers in metal nanocrystals: The effects of shape and field enhancement. *The Journal of Physical Chemistry C*, 118(14):7606–7614, 2014. doi: 10.1021/jp500009k.

[100] X.-T. Kong, Z. Wang, and A. O. Govorov. Plasmonic Nanostars with Hot Spots for Efficient Generation of Hot Electrons under Solar Illumination. *Advanced Optical Materials*, 5(15), aug 2017. ISSN 21951071. doi: 10.1002/adom.201600594.

[101] O. L. Muskens, V. Giannini, J. A. Sánchez-Gil, and J. G. Rivas. Optical scattering resonances of single and coupled dimer plasmonic nanoantennas. *Opt. Express*, 15(26):17736–17746, Dec 2007. doi: 10.1364/OE.15.017736.

[102] F. Wang and Y. R. Shen. General properties of local plasmons in metal nanostructures. *Physical Review Letters*, 97(20):1–4, 2006. ISSN 00319007. doi:

10.1103/PhysRevLett.97.206806.

[103] A. Moreau, C. Ciracì, J. J. Mock, D. R. Smith, R. T. Hill, A. Chilkoti, Q. Wang, and B. J. Wiley. Controlled-reflectance surfaces with film-coupled colloidal nanoantennas. *Nature*, 492(7427):86–89, 2012. ISSN 00280836. doi: 10.1038/nature11615.

[104] M. J. Rozin, D. A. Rosen, T. J. Dill, and A. R. Tao. Colloidal metasurfaces displaying near-ideal and tunable light absorbance in the infrared. *Nature Communications*, 6:1–7, 2015. ISSN 20411723. doi: 10.1038/ncomms8325.

[105] C. Ng, J. J. Cadusch, S. Dligatch, A. Roberts, T. J. Davis, P. Mulvaney, and D. E. Gómez. Hot Carrier Extraction with Plasmonic Broadband Absorbers. *ACS Nano*, 10(4):4704–4711, apr 2016. ISSN 1936-0851. doi: 10.1021/acsnano.6b01108.

[106] S. Mader and O. J. Martin. Mechanisms of perfect absorption in nano-composite systems. *Optics Express*, 26(21):27089, oct 2018. ISSN 1094-4087. doi: 10.1364/OE.26.027089.

[107] G. Kenanakis, C. P. Mavidis, E. Vasilaki, N. Katsarakis, M. Kafesaki, E. N. Economou, and C. M. Soukoulis. Perfect absorbers based on metal–insulator–metal structures in the visible region: a simple approach for practical applications. *Applied Physics A: Materials Science and Processing*, 123(1), 2017. ISSN 14320630. doi: 10.1007/s00339-016-0711-6.

[108] D. Gérard and S. K. Gray. Aluminium plasmonics. *Journal of Physics D: Applied Physics*, 48(18):184001, may 2015. ISSN 0022-3727. doi: 10.1088/0022-3727/48/18/184001.

[109] M. W. Knight, N. S. King, L. Liu, H. O. Everitt, P. Nordlander, and N. J. Halas. Aluminum for Plasmonics. *ACS Nano*, 8(1):834–840, jan 2014. ISSN 1936-0851. doi: 10.1021/nn405495q.

[110] J. Olson, A. Manjavacas, L. Liu, W.-S. Chang, B. Foerster, N. S. King, M. W. Knight, P. Nordlander, N. J. Halas, and S. Link. Full-color aluminum plasmonic pixels. *Proceedings of the National Academy of Science*, 111(40):14348–14353, 2014. doi: 10.1073/pnas.1415970111.